Post-deposition Processing of SnS Thin Films and Solar Cells: Prospective Strategy to Obtain Large, Sintered and Doped SnS Grains by Recrystallization in the Presence of a Metal Ha…

Article *in* ACS Applied Materials & Interfaces · April 2019

DOI: 10.1021/acsami.9b03213

CITATIONS
0

READS
32

7 authors, including:

N. Spalatu
Tallinn University of Technology
31 PUBLICATIONS **81** CITATIONS
SEE PROFILE

Reelika Kaupmees
Tallinn University of Technology
6 PUBLICATIONS **4** CITATIONS
SEE PROFILE

Olga Volobujeva
Tallinn University of Technology
114 PUBLICATIONS **1,517** CITATIONS
SEE PROFILE

Jüri Krustok
Tallinn University of Technology
112 PUBLICATIONS **2,238** CITATIONS
SEE PROFILE

ACS APPLIED MATERIALS & INTERFACES

Research Article

Cite This: ACS Appl. Mater. Interfaces 2019, 11, 17539−17554

www.acsami.org

Postdeposition Processing of SnS Thin Films and Solar Cells: Prospective Strategy To Obtain Large, Sintered, and Doped SnS Grains by Recrystallization in the Presence of a Metal Halide Flux

Nicolae Spalatu,*[,†] Jaan Hiie,[†] Reelika Kaupmees,[†] Olga Volobujeva,[†] Juri Krustok,[‡] Ilona Oja Acik,[†] and Malle Krunks[†]

[†]Department of Materials and Environmental Technology and [‡]Division of Physics, Tallinn University of Technology, Ehitajate tee 5, 19086 Tallinn, Estonia

Supporting Information

ABSTRACT: Postdeposition treatments (PDTs) are common technological approaches to achieve high-efficiency chalcogenide solar cells. For SnS, a promising solar cell material, most PDT strategies to control the SnS properties are overwhelmingly based on an annealing in sulfur-containing ambient atmosphere that is described by condensed-state reactions and vapor-phase transport. In this work, a systematic study of the impact of PDTs in a N_2 atmosphere, ampules at temperatures between 400 and 600 °C, and a $SnCl_2$ treatment at 250−500 °C on the properties of SnS films and SnS/CdS solar cells prepared by close-spaced sublimation is reported. The ampule and N_2 annealing conditions do not affect the grain size of the SnS layers but significantly impact the concentration of intrinsic point defects, carrier density, and mobility. Annealing at 500−600 °C strongly enhances the hole concentration and decreases the carrier mobility, having detrimental impacts on the device performance. $SnCl_2$ treatment promotes grain growth, sintering, and doping by mass transport through the melted phase; it adjusts the hole density and improves the carrier mobility in the SnS layers. SnS/CdS solar cells with an efficiency of 2.8% are achieved in the $SnCl_2$ treatment step, opening new possibilities to further improve the performance of SnS-based devices.

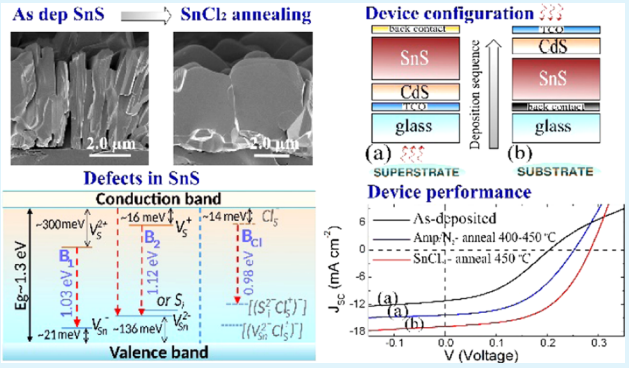

KEYWORDS: *SnS, thin-film solar cells, annealing, melted-phase recrystallization, close-spaced sublimation*

INTRODUCTION

The demand for electricity production with negligible environmental impacts is increasing globally.[1−3] Photovoltaics (PVs) are a nonpolluting and low-maintenance route for generating electricity from the limitless supply of sunlight. However, for PVs to have a considerable impact, lowering the cost of production of solar cells (SCs) is necessary. For decades, thin-film solar cells (TFSCs) have been recognized as important sources of low-cost and environmentally friendly energy for the future.[4] Inorganic TFCSs have achieved very high conversion efficiencies; the copper−indium−gallium−selenide (CIGS) technology reached a record efficiency of 22.9% in 2017,[5] while the CdTe technology obtained a remarkable result of 22.1%[6] in a small area. However, these technologies have some limitations due to the use of toxic or scarce elements as the absorber compounds and difficulties in scaling the automatic fabrication process. Considering these aspects, new absorbers composed of inexpensive, nontoxic, and earth-abundant elements have been investigated, and tin-based chalcogenides have been identified as promising candidates. $Cu_2(ZnSn)(SSe)_4$ (CZTSSe) is one of the most investigated chalcogenide materials, with a record efficiency of 12.6%.[7] However, theoretical studies have revealed several critical issues with CZTS, most of which originate from the multivalence of Sn and the narrow homogeneity range of this multicomponent material.[8]

Orthorhombic tin monosulfide (SnS) has recently emerged as a promising green alternative to CdTe and CIGS solar cells due to its very attractive optoelectronic properties, such as a suitable band gap of approximately 1.3 eV, a high absorption coefficient (10^5 cm^{-1}),[9,10] and an effective onset of optical absorption that coincides with the optimum band gap for maximum efficiency according to the Shockley−Queisser limit within the AM 1.5 illumination of the solar spectrum.[11] In addition, because SnS is a binary compound with a high vapor pressure, a fast, low-temperature, vacuum-based deposition technique can be employed similar to those established in CdTe photovoltaics. Furthermore, the earth-abundant nontoxic constituents and the easy fabrication of these cells promise low-cost manufacturing. All of these attributes suggest

Received: February 26, 2019
Accepted: April 19, 2019
Published: April 19, 2019

DOI: 10.1021/acsami.9b03213
ACS Appl. Mater. Interfaces 2019, 11, 17539−17554

the great potential of SnS for high-efficiency TFSCs and commercial applications. However, in practice, the highest certified power conversion efficiency of SnS devices is still only 4.36%,[12] even though the first SnS PV device was reported in 1997 with a 0.5% efficiency.[13] The current record efficiency has been achieved by following three important approaches: (i) growing p-type SnS by atomic layer deposition (ALD) and subsequent annealing of the absorber in a H_2S ambient atmosphere, (ii) tuning the band offset and carrier concentration in the ALD-Zn(O,S):N buffer layer, and (iii) reducing the interface recombination by the formation of a thin layer ($<\approx$1 nm) of SnO_2 between the absorber and buffer layer.[12] A number of studies have reported SnS devices with efficiencies between 1 and 2%,[9,14−18] which was mainly achieved by refinements in the device design and specific deposition methods rather than by refinements in postdeposition treatments (PDTs). The great deficiency in the open-circuit voltage (V_{OC}) and the poor reproducibility remain the major challenges for SnS TFSCs. For most of the SnS-based devices, V_{OC} values less than 0.25 V have been reported.[14−20] This result could be related to a number of material issues, including (i) low crystalline quality of the single-phase absorber material, i.e., a ribbonlike or layered structure with disordered growth orientations,[21] a high concentration of defects, pinholes, and grain boundaries (GBs),[22] as well as the presence of mixed phases (Sn_2S_3 or SnS_2 polytypes),[23,24] which are detrimental to the PV performance; and (ii) poor device optimization, i.e., lattice mismatch, an unfavorable band offset between p-type SnS and n-type materials, and electrical back contacts.[25,26]

The second issue has been widely investigated by many groups, combining different n-type buffer thin films and varying materials used as electrical contacts.[16−18,25,26] In particular, recent investigations proposed an interesting approach to solve this problem by fabricating SnS solar cells with a p-SnS/n-SnS homojunction configuration,[27] for which the theoretical conversion efficiency is approximately 25%.[28] The first issue appears to be simple in concept but difficult to solve, as it requires improving both the crystal quality (including GBs, interface, and grain interior recombination) and hole density while maintaining a high purity of the SnS phase. The most widely accepted approach to improve the V_{OC} and efficiency of TFSCs is to increase the carrier lifetime by passivating the GBs and/or decreasing their density, employing different procedures for controlling the growth process (using a reactive or inert atmosphere) and different PDTs. For SnS TFSCs, the latest knowledge regarding the novelty and prospects of the kinetically controlled growth of phase-pure SnS absorbers has been reported.[29] Therein, a facile way to modify the shape of orthorhombic SnS grains from vapor transport deposition (VTD) from platelike to more cubelike was demonstrated by controlling the growth pressure during deposition using a flow of inert Ar gas. VTD is a proven, low-cost, and fast-turnaround manufacturing technique for commercial CdTe TFSCs.[30] For the latter, a similar approach has been adopted in a very recent publication,[31] showing that large columnar grains reaching through the entire CdTe layer, a long lifetime, and the potential for improvement of the overall device capability can be achieved by aggressive postdeposition CdTe recrystallization in the presence of a $CdCl_2$ flux. Different PDTs have been tried to improve the crystal quality and the optoelectronic properties of SnS films and solar cells, including annealing in air,[32] vacuum or nitrogen/argon,[9,33] and sulfur-containing ambient atmosphere (H_2S and H_2S/H_2 gas mixture),[9,12,16,22,34−36] with varying degrees of success. Generally, the PDTs have been observed to change grain size and carrier concentration in SnS; however, the results from different reports are often contradictory and lack experimental details and the mechanism by which these treatments induce changes in grain morphology and defect behavior is often not known precisely. Among various PDTs, annealing in H_2S gas has been found to be one of the most efficient approaches for controlling the properties of SnS.[9,12,16,22] It was shown that the treatment stabilizes the sulfur-rich composition of SnS according to the partial pressure of sulfur created by H_2S dissociation;[34] it modifies the grain morphology and adjusts the concentration of majority carrier and intrinsic point defects.[12,16,22,34] Although it was considered one of the key processing steps to achieve the current record efficiency of SnS TFSCs, the annealing requires careful control of H_2S partial pressure to avoid the formation of secondary phases.[9,12,16,22,34−36] Following the example of CdTe and CZTSSe, attempts were also made to improve the crystal quality and the optoelectronic properties of SnS films and solar cells by PDTs in the presence of metal halides and/or alkali additives ($SnCl_2$, $SnCl_4$, KI, NaCl doping),[37−39] but in many cases, these attempts were unsuccessful. Simulating $CdCl_2$ air treatment in CdTe technology, Paudel et al.[37] applied $SnCl_4$ air treatment to improve the SnS device performance; nevertheless, a cell efficiency of 0.1% has been achieved. Di Mare et al.[38] investigated the recrystallization of SnS films by PDT with $SnCl_2$ and KI in the presence of oxygen at 350 and 450 °C, also achieving results below expectations. The failure of these halide treatment procedures that relied on alcohol-based solvents is due to the fact that two very important aspects were neglected: (i) the hydrolysis and oxidation processes, which promote the formation of SnO_2 and oxychlorides during annealing in air, and (ii) the high volatility of $SnCl_2$, which reduces the contribution of $SnCl_2$ to the recrystallization and sintering of SnS grains under open system conditions. In the case of alkali doping procedures,[39] a major drawback is that these procedures are overwhelmingly based on solid-state reactions and vapor-phase transport, which do not provide homogeneous doping of grains and enable them to make contact on the lattice level. Remarkably, given the amount of research into PDT processes, the possibility for a halide−chalcogenide system with the formation of melted phase-assisted recrystallization and doping has rarely been considered, with the exception of recent investigations demonstrating the recrystallization of SnS monograin powders in CdI_2, $SnCl_2$, and KI molten salts.[40] In addition, systematic research related to the influence of the various PDT conditions, including the partial pressure of the system components, the environment, the temperature, and duration of annealing, on the properties of SnS thin films is scarce. A lack of a common understanding of the physicochemical processes behind these treatment steps is an impediment for further development of this promising technology.

Considering these approaches, the aim of the current work was to systematically investigate the influence of different PDT variables, including annealing in a N_2 ambient atmosphere, isothermal treatment in sealed evacuated quartz ampules (with and without a $SnCl_2$ flux), and over a wide range of temperatures, on the structural and optoelectronic properties of close-spaced sublimated (CSS) single-phase SnS thin films and SnS/CdS heterojunction TFSCs.

DOI: 10.1021/acsami.9b03213
ACS Appl. Mater. Interfaces 2019, 11, 17539−17554

It is demonstrated that SnS films with large, sintered, and doped grains and the potential for improvement of the SnS device efficiency overall can be achieved by recrystallization of SnS absorber in the presence of a metal halide flux. A comprehensive understanding on the mechanism and role of melted phase recrystallization, grain growth, sintering, and doping in SnS absorber layer and solar cells during PDT processes in the presence of metal-halide flux is provided. With this systematic approach, we present a new degree of freedom to control the properties of SnS thin films and solar cells to the research community, which can be applied not only to the SnS field but also to other relevant PV materials.

EXPERIMENTAL SECTION

Close-Spaced Sublimation of SnS Thin Films and SnS/CdS Solar Cells. A homemade CSS system was designed and built for this study. The main design requirement for the equipment was that it had to provide a high-purity deposition environment (a description of close-spaced sublimation system for thin-film deposition is given in Figure S1, Supporting Information). Three sets of samples were prepared: SnS single layers on glass substrates, a superstrate configuration of glass/fluorine-doped tin oxide (FTO)/CdS/SnS/Au, and a substrate configuration of glass/Mo/SnS/CdS/i-ZnO/Al:ZnO/Ni/Al heterojunction solar cells. For the SnS/glass structure, the films were grown directly onto chemically and thermally etched 20 × 20 × 1 mm^2 roughened glass plates. Roughened glass plates with a root-mean-square roughness, Rq, of 2.66 nm (O. Kindler) were used to ensure better adhesion of the SnS layers. FTO-coated soda lime glass substrates (Sigma-Aldrich) were used for the fabrication of the superstrate configuration of glass/FTO/CdS/SnS. The typical sheet resistance of the FTO layer was 20 Ω/sq, with a nominal film thickness of 200 nm. Prior to the deposition of the thin films, the 100 × 100 × 2 mm^2 glass/FTO structures were cut into smaller samples with dimensions of 20 × 20 × 2 mm^2 and properly cleaned (the substrate cleaning procedure is given in the Supporting Information). CdS thin films were deposited onto the FTO layer by CSS. The source was a powdered material with 5 N (99.999%) purity (Alfa Aesar). The deposition time, source temperature, and substrate temperatures were kept constant for all CdS layers and were established as 8 min, 590 °C, and 300 °C, respectively. In a standard deposition cycle, the CdS thickness was approximately 80−100 nm. The SnS absorber layers were deposited from SnS source materials with 4 N (99.99%) purity (Testbourne Ltd.). Prior to evaporation, the SnS source material passed the so-called "standardization" preannealing procedure (see the standardization of SnS source material in the Supporting Information). The source temperature, substrate temperature, and deposition time were kept constant at 560 °C, 500 °C, and 2 min, respectively. The SnS absorber layers were typically approximately 2−3 μm thick. For the substrate configuration of glass/Mo/SnS/CdS structures, the SnS films were deposited on Mo/glass substrates under the same conditions as those for the superstrate configuration. After deposition, the SnS/glass, SnS/Mo/glass, and SnS/CdS/FTO/glass structures were cleaved into smaller samples with dimensions of 10 × 10 mm^2 and subjected to a series of thermal treatments under different conditions, which are described below.

Postdeposition Processing of SnS Films and Solar Cells. Thermal annealing of the SnS films and SnS/CdS heterostructures was carried out in a closed process tube in a N_2 atmosphere and in sealed, evacuated quartz ampules. For N_2 annealing, the process tube containing the samples was evacuated; the tube was then filled with 1 atm N_2 gas at room temperature (RT), closed, and introduced into a cylindrical preheated furnace to allow a rapid thermal annealing process. The annealing temperature was varied in the 400−600 °C range, and the annealing time was fixed at 30 min. The N_2 pressure in the process tube was maintained using a standard gas reduction gear and was not influenced by the expansion of the gas at high annealing temperatures. The large diameter (55 mm) and volume (1500 mL) of the process tube ensured an excess of N_2 and gas convection flow so that the reaction products were transported to the colder part of the tube.

Isothermal annealing in sealed, evacuated (∼10^{-3} Torr) quartz ampules was carried out with the samples in the same preheated furnace and over the same temperature interval of 400−600 °C for 30 min. The ampule volumes were typically approximately 10 cm^3. Prior to loading, the ampules were etched in HF/HNO_3, followed by annealing at 1000 °C under dynamic vacuum. For the $SnCl_2$ processing step, a thin layer of $SnCl_2$ ($SnCl_2$ ultradry powder source with 4 N purity, supplied by Alfa Aesar) with a thickness of ∼200 nm was thermally evaporated on top of the SnS absorber, followed by subsequent treatment in the same sealed ampules at temperatures ranging from 250 to 500 °C for 30 min. For all annealing conditions, the ampules and process tube with the samples were allowed to cool in the cold region of the furnace, after the heating system was turned off at the end of the annealing time. Typical cooling time was around 20−30 min to reach 70 °C. Such a cooling profile allowed removal of residual phases of sulfur or $SnCl_2$ and their precipitation in the cold regions of the ampoules/process tube. After cooling to RT, the $SnCl_2$-treated samples were rinsed with deionized water and, in some cases, etched in a standard NP ($H_3PO_4/HNO_3/H_2O$) solution to remove the $SnCl_2$ residue from the SnS surface.

Contact Formation. Different types of back contacts (Au, In) were formed by vacuum evaporation using source materials supplied by Sigma-Aldrich or Alfa Aesar. In and Au with dot contact geometries were used for the Hall measurements of the SnS single layers. For the superstrate configuration of glass/FTO/CdS/SnS, Au back contacts with different geometries were deposited through a mica mask placed between the evaporation source and the sample. A bilayer front contact of i-ZnO and aluminum zinc oxide (AZO) deposited by radio frequency (RF) sputtering (with thicknesses of AZO ∼500 nm and i-ZnO ∼70 nm) were used for the substrate configuration of glass/Mo/SnS/CdS heterostructures. For the latter, a metallic Ni/Al wire grid was applied for improved front contact conductivity.

Characterization of Thin Films and Solar Cells. Surface and cross-sectional views of the samples were obtained using a high-resolution scanning electron microscope to evaluate the SnS surface morphology and SnS/CdS solar cell structure. We used a high-resolution field emission scanning electron microscope Zeiss Merlin equipped with an in-lens secondary electron detector for topographic imaging. Measurements were made at an operating voltage of 2 kV. The chemical composition of the SnS films was determined using an energy-dispersive X-ray (EDX) analysis system Bruker EDX-XFlash6/30. For EDX analysis, an operating voltage of 10 kV were used, and the concentrations of elements were calculated by using PB-ZAF standardless mode. The phase composition and crystallographic properties were analyzed by X-ray diffraction (XRD) on a Rigaku Ultima IV system using monochromatic Cu Kα radiation (λ = 1.5406 Å, 40 kV at 40 mA). Crystal phases were identified using data issued by the Joint Committee on Powder Diffraction Standards. The crystallite sizes and lattice constants were calculated using Rigaku PDXL version 1.4.0.3 software. The Debye−Scherrer formula was used to calculate the crystallite size.

Room-temperature Raman spectra were recorded in a 180° backscattering geometry using Horiba's LabRAM HR high-resolution spectrometer. The incident laser light with a wavelength of 532 nm was focused on the sample within a spot of diameter 10 μm, and the spectral resolution of the spectrometer was approximately 1.5 cm^{-1}.

A 0.64 m focal length single-grating (600 mm^{-1}) monochromator and the 442 nm line of a He−Cd laser power of 37.1 mW were used for the photoluminescence (PL) measurements. A closed-cycle helium cryostat was employed to measure the temperature dependencies of the PL spectra at temperatures from 10 to 300 K. The PL signal was detected by an InGaAs detector.

The resistivity, charge carrier concentration, and mobility of the SnS films were measured at RT using MMR's variable-temperature Hall system and a Hall and van der Pauw controller H-50. The in-plane resistivity and hole densities were calculated for thicknesses of

DOI: 10.1021/acsami.9b03213
ACS Appl. Mater. Interfaces 2019, 11, 17539−17554

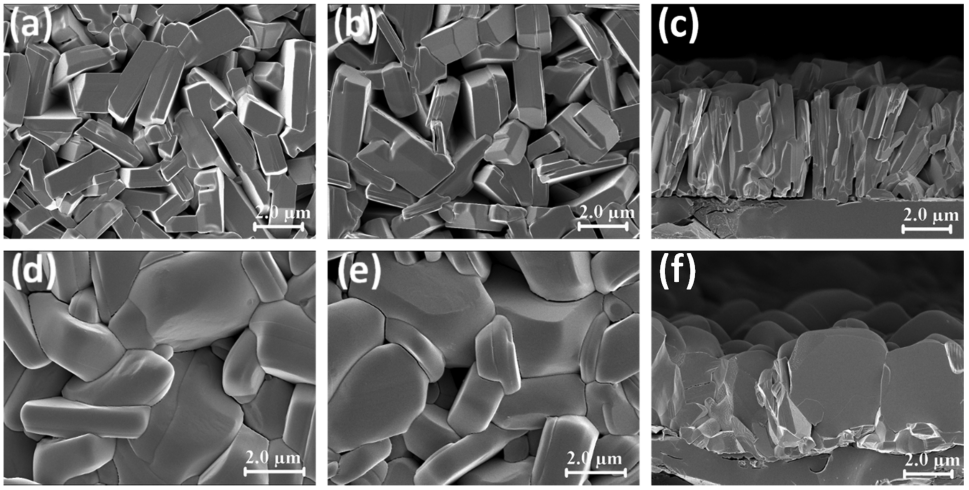

Figure 1. SEM images of CSS SnS films grown on glass substrates at 500 °C: (a) as-deposited films; (b) AMP-annealed at 500 °C for 30 min; (c) cross-sectional view of as-deposited films; (d) $SnCl_2$-annealed at 450 °C; (e) $SnCl_2$-annealed at 500 °C; and (f) cross-sectional view of $SnCl_2$-annealed at 450 °C.

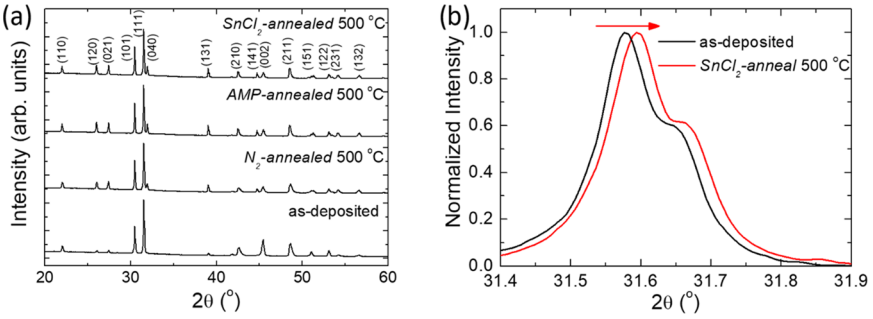

Figure 2. (a) XRD patterns of SnS thin films before and after the PDT processes. (b) Displacement of the (111) XRD peak of $SnCl_2$-annealed SnS films at 500 °C for 30 min. The double structure of the (111) peak is due to the Kα_2 line.

2−3 μm, which were estimated from the SEM analysis. Each measurement was carried out 10 times and the mean value was taken.

For cell characterization, we used the current−voltage characteristics (J−V) and the external quantum efficiency (EQE) spectra. The J−V curves were measured under standard white light with an illumination intensity of 100 mW/cm^2 (AM 1.5) using the four-point probe technique on an AUTOLAB PGSTAT 30 and Oriel class A solar simulator 91159A. The EQE was measured in the spectral region of 300−1000 nm using a computer-controlled SPM-2 monochromator (Carl Zeiss-Jena) and a 300 W Xe lamp as the excitation light source. The dispersed light from the Xe lamp incident on the solar cell as monochromatic light was optically chopped at 30 Hz.

RESULTS AND DISCUSSION

Influence of PDT Processing Conditions on the Properties of SnS Thin Films. *Structural Properties.* As described in Experimental Section, our experiments involved three different PDT processes: (i) thermal annealing in sealed quartz ampules at temperatures from 400 to 600 °C for 30 min; (ii) annealing in the processing tube under a N_2 atmosphere from 400 to 600 °C for 30 min; and (iii) $SnCl_2$ treatment in sealed ampules from 250 to 500 °C for 30 min. For reference, the SnS films annealed with the conditions in (i) were labeled as AMP-annealed, those annealed with the conditions in (ii) were labeled as N_2-annealed, and those annealed with the conditions in (iii) were labeled as $SnCl_2$-annealed. Each sample that was subjected to annealing had a reference as-deposited sample cleaved from the same substrate. This approach allowed us to systematically follow the changes in the properties of the SnS films induced by the PDT processes.

Figure 1a−f shows the top- and cross-sectional-view SEM images of the SnS/glass samples before and after the PDT processes. The deposited films consisted of platelike-shaped large grains with size between 1 and 2 μm, aligned perpendicular to the substrate, with a relatively high density of GBs. The growth followed the layered crystal structure of orthorhombic SnS, which is frequently observed in SnS growth by other methods due to the anisotropic growth rates of the planes.[14−22,29] There were no evident changes in the morphology and thickness of the SnS films after the AMP-annealing and N_2-annealing processes (Figures 1b and S2 in the Supporting Information). The energy-dispersive X-ray spectroscopy (EDS) analysis (not shown) of the as-deposited SnS indicates a stoichiometric composition, and after any of the annealing steps, no detectable changes in stoichiometry were observed. The morphology of the SnS thin films changed dramatically after the $SnCl_2$-annealing step.

The surface of the chloride-treated layers at 250 °C (Figure S3 in the Supporting Information) preserves the same structure with platelike-shaped large grains and penetrating boundaries. SnS films treated at 300 and 350 °C had relatively large grains (2−3 μm) with irregular forms, traversing holes, and neck regions between the coalesced grains (Figure S3, Supporting Information). In the case of the SnS films annealed

DOI: 10.1021/acsami.9b03213
ACS Appl. Mater. Interfaces 2019, 11, 17539−17554

at 450−500 °C, it appears that the $SnCl_2$ treatment further increased the grain size up to 3−4 μm and induced sintering of grains, which significantly decreased the number of intergranular pores/density of voids, resulting in films with a close-packed morphology (Figure 1d−f).

Figure 2a displays the X-ray diffraction (XRD) patterns of SnS films deposited on glass substrates before and after the PDT processes. All of the films are polycrystalline, preferably oriented along the (111) direction with dominant diffraction peaks corresponding to the orthorhombic SnS crystal structure (PDF card no: 01-075-1803) and matching well with those reported in the literature for SnS films deposited by the CSS and VTD techniques.[29,37,41] In addition, a peak corresponding to the (040) plane of SnS was observed for all layers.

It is well known that the growth methods determine whether the polycrystalline SnS thin films have a dominant (111) or (040) orientation. A number of studies have reported SnS films grown by high-vacuum evaporation and sputtering methods with flakelike-shaped small grains and the (040) preferred orientation.[17,33,36,42] The differences in the grain size, shape, and orientation of the SnS films obtained by different physical deposition methods can be explained by differences in the nucleation density and coalescence rates in the deposition system. In the case of CSS, nucleation takes place via a vapor−solid phase transition.[43,44] The molecules condense onto the surface of the substrate (called adatoms), and an initial set of nuclei is formed by deposition from the vapor phase. Nuclei that are stable enough for reevaporation continue to grow by the addition of material from the vapor and by the surface diffusion of adatoms, thus forming islands. Ostwald ripening and coalescence are assumed to be the dominant processes in thin-film formation.[43] All of these processes depend on the temperature gradient (source−substrate temperature) and vapor pressure in the CSS system. At a high substrate temperature of 550 °C, as in our case, the adatom mobility and surface diffusion are high, leading to fewer nucleation sites. The small temperature gradient between the source and substrate (50−70 °C) and the high vapor pressure of SnS in the CSS system leads to the orientation of the crystallites along the planes with the highest growth rate; for the orthorhombic (distorted cubic) SnS, these planes are the densely populated (111) planes. Orientation selection during the coalescence stage is more pronounced, as it is driven by a decrease in the total GB area as well as by minimization of the interfacial and surface energies.[43] Thus, large platelike SnS grains with low surface energies grow in both perpendicular and lateral directions, i.e., the creation of (040) planes bonded by van der Waals forces with the lowest surface energy.[22,36]

The XRD patterns do not show any evident changes for $SnCl_2$-annealed SnS films. Furthermore, no secondary phases were detected in the films, either after treatment alone or after the etching procedure (Figure 2a). To understand the impact of PDT processing conditions on the structural properties of SnS thin films, we further analyzed the changes in the crystallite sizes and lattice parameters of the films. The crystallite size and lattice parameter values are listed in Table 1. The deposited SnS films had a large crystallite size of approximately 104 nm, indicating a high degree of crystallinity. Subsequently, the AMP-annealing process at 400 °C slightly increased the crystallite size up to 107 nm, and a further gradual increase in the temperature to 600 °C assured a systematic increase in the crystallite size of SnS films from 107 to 117 nm (Table 1). Considering the small volume of the ampule (~10 cm^3) and the closed isothermal conditions in the AMP-annealing step, this effect can be explained as being generated by the low mass-transport rate in the solid and gas phases, promoting slow crystallite growth. However, this effect was not observed in N_2-annealed films in which the processing tube has a significantly larger nonisothermic volume that inhibits this process.

Table 1. Average Crystallite Size (D) and Lattice Parameter (a_0) of SnS Films Depending on the PDT Processing Conditions

			a_0 (Å) (±0.001)		
PDT conditions	T (°C)	D (nm)	a	b	c
as-deposited		104	4.319	11.199	3.992
AMP-annealed	400	107	4.319	11.189	3.985
	500	112	4.322	11.180	3.983
	600	117	4.326	11.180	3.983
N_2-annealed	400	104	4.314	11.190	3.986
	500	106	4.321	11.182	3.981
	600	103	4.325	11.180	3.981
$SnCl_2$-annealed	250	120	4.326	11.190	3.983
	350	135	4.327	11.183	3.983
	450	150	4.329	11.174	3.980
	500	130	4.329	11.174	3.973

As a result of the $SnCl_2$-annealing step from 250 to 450 °C, the crystallite size of the SnS films increased systematically from 120 to 150 nm (Table 1). Further increasing the temperature to 500 °C slightly decreased the crystallite size to 130 nm. At the same time, we observed side effects from 500 °C annealing, such as the precipitation of white-gray SnS−$SnCl_2$ (confirmed by EDS) in the cold regions of the ampoules (for annealing temperatures ≤450 °C, only white $SnCl_2$ residuals were detected). SEM analysis showed a decrease of film thickness from 3 μm for as-deposited samples to 2.2−2.5 μm after the same annealing temperature. This result indicated that 500 °C was the critical temperature at which the mass transport and resublimation of the $SnCl_2$ flux and SnS main material occurred, so actively that significantly decreases the thickness of the films. At 500 °C, the vapor pressure of SnS is about 10^{-2} Torr,[45] and it starts to sublimate quite intensively in the CSS system. At the same temperature, the vapor pressure of $SnCl_2$ is very high (>30 Torr) and the eutectic of the SnS−$SnCl_2$ system is lower than 247 °C.[46] Under these conditions, considering fast cooling profile used in our experiments, the $SnCl_2$ vapor flux carries the SnS in the cold part of the ampoule and hence the film thickness decreases.

An interesting phenomenon was observed for SnS films that passed the AMP-annealing and N_2-annealing steps, in which the lattice parameters along the b and c axes decrease systematically, while along the a axis, a gradual increase was observed (Table 1). This effect was accompanied by the displacement of the main (111) XRD peak and was more pronounced for $SnCl_2$-annealed layers, especially at high temperatures of T = 450−500 °C (Figures 2b and S4 in the Supporting Information). Thus, after the $SnCl_2$-annealing step at 450−500 °C, high-resolution analysis demonstrated a shift of the (111) peak toward higher 2θ values, corresponding to the decrease in the lattice parameter along the b axis from 11.199 to 11.174 Å (Table 1). A similar phenomenon previously observed for the (111) peak in the $CdCl_2$-activated CdTe films that was explained by the incorporation of chlorine at tellurium sites (with chlorine having a smaller ionic radius

DOI: 10.1021/acsami.9b03213
ACS Appl. Mater. Interfaces 2019, 11, 17539−17554

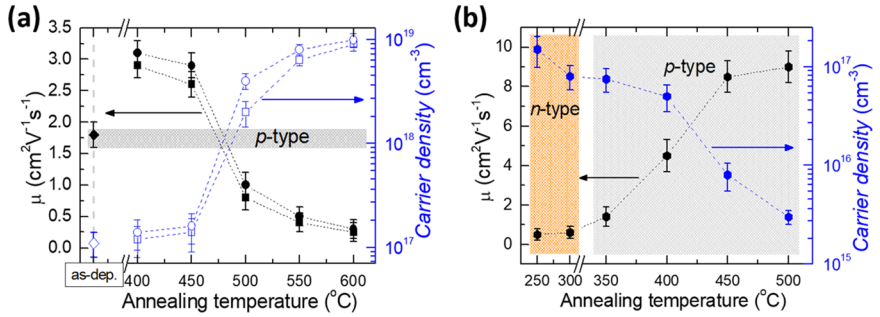

Figure 3. RT hole concentration and hole mobility in SnS films: (a) AMP-annealed (μ—●; p—○) and N_2-annealed (μ—■; p—□) at temperatures between 400 and 600 °C for 30 min (average values for ∼60 samples); (b) after $SnCl_2$ annealing at 250−500 °C for 30 min (average values for ∼30 samples).

than tellurium; Cl^-: 167 pm, Te^{2-}: 221 pm) together with the formation of cadmium vacancies causing contraction of the CdTe sublattices.[47,48] Analogous to CdTe, assuming the incorporation of $SnCl_2$ into the SnS lattice, we explain the shift of the (111) peak shown in Figure 2b by the presence of chlorine at the sulfur sites and the formation of tin vacancies. The ionic radius of chlorine (Cl^-: 167 pm) is smaller than the ionic radius of sulfur (S^{2-}: 184 pm),[49] and thus, together with the tin vacancies (V_{Sn}), they cause a contraction of the SnS sublattices and a decrease in the lattice parameter.

An explanation of the changes in the lattice parameters of SnS films induced by the AMP-annealing and N_2-annealing steps at 400−600 °C is based on the sulfur-rich composition of the SnS films. Indeed, according to the phase diagram of the Sn−S system,[50] there is a tendency for the formation of sulfur-rich compositions with concentrations lower than 1% (below the detection limit of XRD and Raman spectroscopy). Rau[34] experimentally measured the equilibrium pressures and amounts of sulfur from the SnS crystals between two consecutive pressure values along the three-phase lines, including the solid-phase SnS for temperatures of 560−600 °C, and obtained a sulfur-rich composition with excess sulfur concentrations between 10^{17} and 10^{18} cm^{-3}. Considering the extremely low vapor pressure of Sn above the metal phase (<10^{-5} Torr) and the low SnS fraction in the vapor phase (<7 Torr, i.e., ∼25% of the total pressure of SnS, S_2, and Sn) at the SnS melting point (881 °C),[50] the sulfur pressure predominates over the entire investigated SnS composition temperature range. In other words, the SnS homogeneous domain is always situated in the sulfur-rich region relative to the stoichiometric compound. Under these conditions, the increased partial pressure of sulfur (especially for isothermal conditions of the AMP-annealing step at 500−600 °C) generates more tin vacancies (V_{Sn}) and probably generates interstitial sulfur (S_i), thus promoting rearrangement of the SnS lattice along the *a*, *b*, and *c* axes (Table 1).

The dependence of the phase composition of SnS thin films on the PDT processing conditions was also analyzed by Raman spectroscopy. Figure S5 in the Supporting Information shows the characteristic Raman modes at 95, 165, 193, and 219 cm^{-1}, commonly observed for orthorhombic SnS films.[15,29,33] No vibrational peaks were detected at 302 and 310 cm^{-1} belonging to the SnS_2 or Sn_2S_3 secondary phases, neither for the as-deposited films nor after any of the PDT processes, indicating the presence of pure-phase SnS thin films. At the same time, a shift in the peak positions toward lower energies was observed for $SnCl_2$-annealed films (Figure S5b, Supporting Information). This type of red shift in the Raman peak position indicates the presence of tensile strain in the films.[51] Considering the chloride treatment step, this phenomenon can be explained by the development of internal stress in the films and/or compressive strain generated by the lattice and thermal mismatch between SnS and the underlying substrate during the grain growth and sintering processes.

Based on the obtained results, we claim that the $SnCl_2$ treatment induces the formation of liquid flux and mass transport through the melted phase, promoting grain growth by recrystallization and sintering in the SnS films. The grain growth is accomplished by the incorporation of flux components into the growing SnS lattice. According to the phase diagram of the SnS−$SnCl_2$ system,[46] enhanced mass transfer and recrystallization of SnS through the liquid phase can be expected for temperatures higher than the eutectic temperature (∼246 °C). At these temperatures, melted solutions of SnS in $SnCl_2$ with high concentrations of SnS will form. The liquid-phase recrystallization of SnS films during the $SnCl_2$ treatment can be explained as follows. When the ampule with SnS films coated with $SnCl_2$ is placed into the preheated furnace, some time is required to reach the equilibrium composition of the flux solution and achieve uniform distribution of the liquid phase in the intergranular spaces. In the first step of the process, the intergranular capillaries are filled with the formed liquid phase of the flux, which promotes grain growth by Ostwald ripening.[43] Because of the fast evaporation of $SnCl_2$, the volume of the flux decreases, and the grains are compressed by the capillary contracting force created by surface tension on the liquid-phase meniscus between the contacting grains, leading to sintering of the grains and good contact between them. The degree and rate of liquid-phase sintering depend on the temperature and time and are inversely proportional to the dimensions of the initial SnS grains. Thus, a higher annealing temperature and smaller grains (high surface energies) result in a more intense recrystallization and grain growth by mass transport through the melted flux. At higher temperatures (450−500 °C), larger SnS grains with lower surface energies grow in both perpendicular and lateral directions, leading to the formation of a dense, continuous, and pore-free SnS thin film (Figure 1d−f). At the same time, to avoid the fast evaporation of $SnCl_2$ (vapor pressure at 400−450 °C is ∼22.5 Torr[46]) and its loss before the formation of liquid phase and starting of the sintering process, a rapid thermal annealing profile should be used.

Compared to H_2S annealing at 400−450 °C,[9,12,16,22,34−36] where the grain growth is slow due to the low vapor pressure of SnS, ∼10^{-5} Torr[36,45] at these temperatures (corresponding to

DOI: 10.1021/acsami.9b03213
ACS Appl. Mater. Interfaces 2019, 11, 17539−17554

the low concentration of SnS in the vapor phase), the mass transport and grain growth rate in the presence of melted solution of SnS in liquid $SnCl_2$ (flux) is very high, due to the high solubility of SnS in $SnCl_2$ (about 10 atom %[46]). It is well known that the diffusion rate in the melted flux is about 5 orders of magnitude higher than in solid phase. Considering these aspects, $SnCl_2$ treatment is a feasible processing step to obtain SnS films with large, columnar, and sintered grains.

Electrical Properties. To investigate the impact of the PDT processing conditions on the electrical properties of SnS films, van der Pauw resistivity and Hall effect measurements were carried out at room temperature for a series of ~100 samples. Figure 3a displays the carrier density and Hall mobility of SnS films after the AMP-annealing and N_2-annealing steps at 400−600 °C for 30 min. For both annealing conditions, 10 samples were used for each processing temperature and the average values are presented.

The as-grown films always exhibited p-type conductivity with a resistivity of 10−15 Ω cm, a carrier density of $\sim 10^{17}$ cm^{-3}, and a Hall mobility of 1.8 ± 0.3 $cm^2/(V\ s)$. Similar values of the hole concentration have been reported by Albers et al.[52] for SnS single crystals and by Yanuar et al.[41] for SnS films grown by close-spaced vapor transport at 500 °C. Generally, for most of the orthorhombic p-type SnS films grown by different techniques, including physical deposition methods such as sputtering,[36] pulsed laser deposition,[53] vacuum evaporation,[10] and chemical methods, including spray pyrolysis[9] and chemical bath deposition,[54] typical values of the hole concentration between 10^{13} and 10^{15} cm^{-3} are reported.

The changes in the hole density of SnS films induced by the AMP-annealing and N_2-annealing steps in the temperature range of 400−600 °C can be divided into two intervals. The first interval at 400−450 °C is characterized by a small but gradual increase in the hole concentration to a level of $(2-4) \times 10^{17}$ cm^{-3} and the hole mobility up to 3 ± 0.3 $cm^2/(V\ s)$. In the second interval at 500−600 °C, the hole density increased abruptly to 10^{19} cm^{-3} and a sharp decrease in hole mobility was observed (Figure 3a).

A reduction in the SnS film resistivity with the development of a high hole density ($\sim 10^{19}$ cm^{-3}) after 30 min of annealing at 500−600 °C represents the most striking result. These carrier concentration values in the absorber layer might crucially influence the quality of the p−n heterojunction in a SnS/CdS solar cell. Therefore, it is extremely important to explain the physicochemical mechanism behind the changes in the SnS electrical properties. These phenomena can be explained considering the previously mentioned claim that solid SnS contains excess sulfur. According to Piacente et al.,[45] SnS molecules do not dissociate in the vapor phase, i.e., the dissociation constant is very low, and the evaporation of SnS occurs according to eq 1

$$SnS_{(s)} \leftrightarrow SnS_{(g)} \tag{1}$$

Sulfur-rich conditions can be understood as a solid solution of molecular sulfur in SnS, accompanied by the formation of tin vacancies, V_{Sn} (eq 2)

$$nS_{2(g)} + SnS_{(s)} \leftrightarrow [Sn_{(1+n)}S_{(1+2n)}2nV_{Sn}]_{(s)} \tag{2}$$

It is widely accepted that V_{Sn} acts as a shallow acceptor and is mainly responsible for the p-type conductivity of SnS.[50,52] Taking into account the isothermal conditions of the AMP-annealing step and the nitrogen contrapressure in the N_2-annealing process step, a high vapor pressure of sulfur above that of SnS promotes an increase in the concentration of $[V_{Sn}]$. The higher the annealing temperature, the higher the sulfur partial pressure above that of SnS and the greater the concentration of tin vacancies $[V_{Sn}]$, leading to an increased hole density. The sulfur overpressure contributes to the rebuilding of the sulfur sublattice by decreasing the overall concentration of sulfur vacancies (V_S, donor defect[53]), and the tin sublattice responds with the formation of tin vacancies to reach equilibrium in the crystal. The formation of Schottky defects and the equilibrium constant in the SnS lattice are given below.

1. Formation of intrinsic vacancy defects

$$V_{Sn}^{2-} + V_S^{2+} = 0 \tag{3}$$

$$K_{Scottky} = [V_{Sn}^{2-}]\cdot[V_S^{2+}] \tag{4}$$

Incorporation of sulfur

$$1/2S_{2(g)} = V_{Sn}^{2-} + S_s + 2h,\ \text{h—hole} \tag{5}$$

Generation of holes

$$V_{Sn}^{0} \leftrightarrow V_{Sn}^{-} + h\ \text{(ionization at room temperature)} \tag{6}$$

$$V_{Sn}^{-} \leftrightarrow V_{Sn}^{2-} + h\ \text{(ionization at high annealing temperatures)} \tag{7}$$

Mass action law and electroneutrality condition

$$n\cdot p = n_i^2 = \text{const} \tag{8}$$

$$[V_{Sn}^{2-}] + n = [V_S^{2+}] + p\ \text{(at high annealing temperatures)} \tag{9}$$

$$n \ll p \rightarrow [V_{Sn}^{2-}] = p,\ \text{p-type conductivity determined by doubly ionized tin vacancies at high annealing temperatures} \tag{10}$$

According to Rau,[34] the first ionization energy of V_{Sn} is very low (~20 meV), so the hole concentration in SnS at room temperature is dependent on the concentration of $[V_{Sn}]$ in the lattice. The energy of the second ionization step is approximately 0.2−0.3 eV, and due to the association of V_{Sn} in the lattice, the hole concentration in SnS is low, corresponding to a high resistivity at the lowest pressure of sulfur, which is determined by the homogeneity region.[34]

Another way to study the increased density of holes in SnS films after the AMP-annealing and N_2-annealing steps at 400−600 °C can be achieved following the model of the association−dissociation of tin vacancies proposed by Albers et al.[52] for SnS single crystals, within the same approach of sulfur-rich condition

$$2h + 2V_{Sn}^{-} \leftrightarrow (V_{Sn}V_{Sn})^{\times} \tag{11}$$

$$4h + 2V_{Sn}^{2-} \leftrightarrow (V_{Sn}V_{Sn})^{\times} \tag{12}$$

Assuming that the $(V_{Sn}V_{Sn})$ neutral complex acts neither as a donor nor as an acceptor, the concentration of holes in the SnS films depends only on the annealing temperature, time, and cooling rate due to the dissociation of neutral centers, resulting in an increased concentration of V_{Sn} capable of ionizing at room temperature. Considering the high cooling rate used in

DOI: 10.1021/acsami.9b03213
ACS Appl. Mater. Interfaces 2019, 11, 17539−17554

our experiments, the concentration of ionized tin vacancies (which determines the hole density measured at room temperature) reflects the values of $[V_{Sn}]$ generated at the annealing temperature. The high cooling rate (quenching) is a common approach used in thin-film technologies to examine the properties of the layers at the annealing temperature. On the other hand, as shown in the Structural Properties section, the rapid thermal annealing is also very important to control the morphology and concentration of defects in SnS films (especially for $SnCl_2$-annealing step). Thus, to control the hole concentration in SnS by annealing, the crucial conditions are the sulfur pressure at the annealing temperature, thermal annealing, and cooling profile of the sample. Compared to Albers et al.,[52] the hole density in the AMP/N_2-annealed SnS films did not change significantly at annealing temperatures below 500 °C (Figure 3a), while in the single crystals, the hole concentration increased by more than 1 order of magnitude (from (5×10^{16}) to 10^{18} cm^{-3}) at temperatures between 200 and 400 °C. In our case, the SnS films were deposited at 500 °C, allowing large grain growth with the corresponding concentration of $[V_{Sn}]$ for these conditions. Because the concentration of defects was already established during the film deposition at 500 °C, very little change in the defect concentration could occur during the subsequent AMP-annealing and N_2-annealing steps at lower temperatures of 400−500 °C. As the hole density increased with increasing annealing temperature, the Hall mobility decreased systematically from 3 to 0.2 $cm^2/(V\ s)$ (Figure 3a). This behavior is explained by the scattering of carriers through ionized tin vacancy defects with high concentrations at elevated temperatures.

We next investigated the changes in the electrical properties of SnS films induced by the $SnCl_2$-annealing step from 250 to 500 °C. An interesting effect was observed for $SnCl_2$-treated films annealed at 250 and 300 °C: the films exhibited n-type conductivity with a resistivity of $(1-2.5) \times 10^2$ Ω cm, an electron density of $(6 \times 10^{16})-10^{17}$ cm^{-3}, and a Hall mobility of 0.25−0.85 $cm^2/(V\ s)$ (Figure 3b). These changes in the electrical properties are stable to the subsequent etching procedure, indicating that they occur in the bulk of the polycrystalline material and not only at the SnS film surface. Starting at 350 °C, the films showed p-type conductivity, and a further increase in the $SnCl_2$-annealing temperature resulted in a systematic decrease in the hole density. In contrast, the Hall mobility increased from 1.5 to 9 $cm^2/(V\ s)$ as the $SnCl_2$ annealing temperature was increased from 350 to 500 °C (Figure 3b). The changes in the electrical properties of $SnCl_2$-annealed SnS films can be explained based on the incorporation of $SnCl_2$ into the SnS layers, as already presented in the Structural Properties section.

Chlorine seems to incorporate into SnS at the sulfur site, similar to the scheme of Cl_S and Cl_{Te} incorporation into CdS and CdTe, respectively, acting as a shallow donor.[47,55,56]

$$SnS_{(s)} + nSnCl_{2(l)} \leftrightarrow [(1+n)Sn_{Sn}S_S nV_{Sn}(2n)Cl_S]_{(s)} \quad (13)$$

Each $SnCl_2$ molecule generates one V_{Sn} for every pair of incorporated Cl_S (eq 13). As a result, the double-charged acceptor V_{Sn}^{2-} is compensated by the Cl_S^+ shallow donors. Additionally, a neutral defect $(V_{Sn}2Cl_S)^\times$ can be formed at high concentrations of dopant, and as a result of $(V_{Sn}2Cl_S)^\times$ dissociation (eq 14), the created shallow acceptor defect $(V_{Sn}Cl_S)^-$ compensates the Cl_S^+ shallow donor so that the $SnCl_2$-treated SnS films can behave as n- or p-type semiconductors depending on the ratio of $[V_{Sn}]/[Cl_S]$.

$$(V_{Sn}2Cl_S)^\times \leftrightarrow (V_{Sn}Cl_S)^- + Cl_S^+ \quad (14)$$

As shown, grain growth takes place by mass transport through the liquid flux. The equilibrium between the liquid flux and the solid SnS determines the rate of chlorine doping according to the distribution coefficient (K_d) between the liquid and solid phases at the processing temperature (eq 15)[48,57]

$$K_d = C_s/C_l \quad (15)$$

where $C_s \approx 10^{19}$ cm^{-3} and $C_l \approx 10^{22}$ cm^{-3} are the estimated chlorine concentrations in the solid and liquid fluxes, respectively. This high value of $K_d \approx 10^{-3}$ corresponds to the incorporation of the saturated chlorine concentration into the lattice of growing SnS and at the GBs, which is assured by the limitless supply of chlorine in the liquid flux. Although the etching procedure removed the residual $SnCl_2$ from the surfaces of the SnS films (in Figures 2a and S5 (Supporting Information), the XRD and Raman results did not show any secondary phases), the residual in the GBs could not be eliminated completely. Presumably, high concentrations of residuals strongly limit the density of charge carriers in p-type SnS by self-compensation and could cause hygroscopicity of the solar cells.

Segregation of residual impurities at the GBs is also common for other TFSC PV technologies, such as CIGS or CdTe. For CdTe, segregation of the $CdCl_2$ and $CdCl_2{\cdot}2CdO$ residual phases at GBs with a concentration of $\sim 10^{19}$ cm^{-3} was observed by transmission electron microscopy and secondary-ion mass spectroscopy analysis after $CdCl_2$ activation treatment,[58−60] which is the key processing step to achieve high-efficiency CdTe cells. The high resistivity and conversion from p- to n-type conductivity of the $SnCl_2$-annealed SnS films at 250 and 300 °C suggest that the $SnCl_2$ treatment left a high concentration of chlorine in the films. It is likely that the low annealing temperatures and high cooling rate promote conditions for the segregation of chloride residuals at GBs. This process leads to an increase in the concentration of Cl_S^+ shallow donors and neutral $(V_{Sn}2Cl_S)^\times$ complex defects and results in n-type conductivity of the SnS films. The small Hall mobility values in these films (0.45−0.65 $cm^2/(V\ s)$, Figure 3b) are consistent with previously reported values in Cl-doped SnS single crystals and can be explained via ionized impurity scattering, which is assumed to be the dominant scattering mechanism in chlorine-doped n-type SnS ceramics.[27,61] It should also be noted that the carrier-type conversion from p- to n-type in polycrystalline SnS ceramics has been observed for Cl-doping concentrations lower than 0.3%.[61]

In $SnCl_2$-treated films at higher temperatures (especially at 450 and 500 °C), the chlorine concentration seemed to be more balanced with the concentration of native $[V_{Sn}]$ defects. Indeed, considering the high annealing temperatures, a longer time is needed for cooling to room temperature, and the longer exposure time of samples at high temperatures promotes conditions for the out-diffusion of residual and excess chlorine from SnS films. Because of the lower amount of chlorine in these films, the concentrations of $[V_{Sn}^-]$ and $[(V_{Sn}^{2-}Cl_S^+)^-]$ shallow acceptors increase and the p-type properties and mobility improve (Figure 3b). These results indicate the possibility for a subsequent treatment procedure under a temperature gradient to allow the gathering of $SnCl_2$ residuals

DOI: 10.1021/acsami.9b03213
ACS Appl. Mater. Interfaces 2019, 11, 17539−17554

from SnS layers, hence enabling control of their p-type doping properties.

Photoluminescence Study. To confirm the aforementioned statements, we measured the photoluminescence (PL) spectra at 10 K of SnS films as a function of the PDT processing conditions. Generally, there are a very limited number of reports in the literature on PL studies of SnS films deposited by physical deposition techniques. Referring to the solution-based deposition methods, the first report of PL investigations was published by Sajeesh et al.[62] and had a major impact for SnS films deposited by chemical spray pyrolysis (CSP). A number of studies have employed PL analysis in nonconventional quantum dot SnS nanoparticle hybrid structures for application in battery-based storage systems and photocatalytic activities.[63,64] The limited number of PL reports on conventional SnS-based thin-film structures seems to be related to the complex nature of this material, i.e., the indirect and direct band gap dual behavior of SnS and the difficulties in attaining single-phase SnS material with a high crystalline quality and a low concentration of defects and GBs by different methods.

Figure 4a,b shows the PL spectra at 10 K for the as-deposited, AMP-annealed, and N_2-annealed SnS films at 400–600 °C for 30 min. For both the as-grown and annealed films, the PL spectra exhibited a broad asymmetric emission band at approximately 1.03 eV. At the same time, different features in the PL spectra were found to be characteristic of a distinct annealing temperature range. Thus, for both N_2 and ampule annealing conditions, with increasing temperature, the intensity of the 1.03 eV PL band slightly decreases, and starting at 500 °C, a new PL band appears at higher energies. The prevalence of one or the other emission band was determined by the annealing temperature. The 1.03 eV emission band prevailed at 400–500 °C annealing temperatures, whereas at 550–600 °C, the 1.12 eV band predominated. The appearance of a 1.12 eV emission band at high annealing temperatures is the most striking result. For the same temperature interval, we observed an abrupt increase in the hole concentration of SnS films (Figure 3a). Therefore, it is important to find the correlation between these two phenomena and to explain the mechanism by which the annealing step induced these changes.

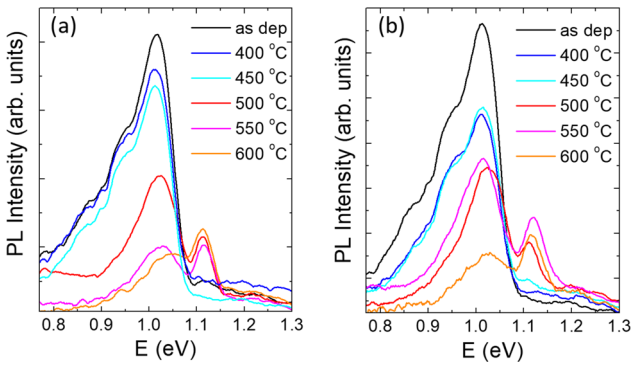

Figure 4. Low-temperature PL spectra of SnS films vs (a) AMP-annealed from 400 to 600 °C for 30 min and (b) N_2-annealed from 400 to 600 °C for 30 min.

Figure 5a,b shows the PL spectra of the SnS films after the AMP-annealing and N_2-annealing steps at 500 °C for 30 min. We have found that acceptable agreement between the experimental data and the fit can be achieved by assuming

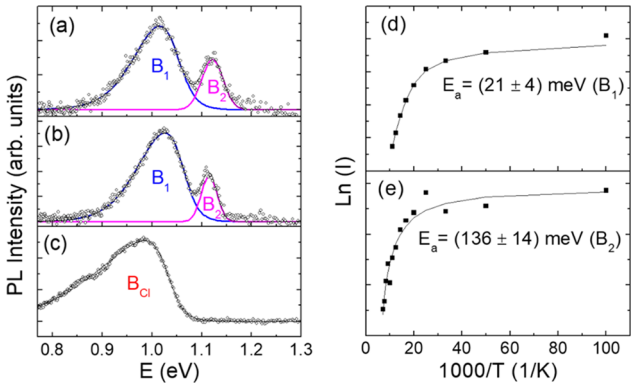

Figure 5. Low-temperature PL spectra of SnS films vs PDT conditions: (a) AMP-annealed at 500 °C for 30 min, (b) N_2-annealed at 500 °C for 30 min, (c) $SnCl_2$-annealed at 500 °C for 30 min, and (d, e) Arrhenius plots of the integral intensity of the B_1 and B_2 PL bands with the fitting results, respectively.

that there are two peaks. Thus, two PL bands (B_1 and B_2) are clearly distinguished at approximately 1.03 and 1.12 eV, respectively. The energetic distance between the B_1 and B_2 PL bands was approximately 90 meV. To determine the thermal activation energies (E_A) of the B_1 and B_2 PL bands, the temperature dependence of PL emission was analyzed. Arrhenius plots of the resulting integral intensities for both bands are shown in Figure 5d,e. The best fits were achieved using a model[65] in which the temperature dependence of the hole capture cross section was taken into account (eq 16)

$$I(T) = I_0/[1 + A_1T^{3/2} + A_2T^{3/2}\exp(-E_a/kT)] \quad (16)$$

where I is the integral intensity of the PL band, I_0 is the intensity at 0 K, A_1 and A_2 are process rate parameters, and E_a is the activation energy. The obtained activation energies E_a for the B_1 and B_2 bands were 21 ± 4 and 136 ± 14 meV, respectively.

The B_1 emission band has been observed previously by Sajeesh et al.[62] for CSP SnS films, and the obtained value for the activation energy was ~20 meV. Therein, a donor–acceptor pair (DAP) recombination involving a shallow donor at 20 meV and a deep acceptor at 0.22 eV was also proposed. It is well established that, as a rule, the recombination rate of DAPs exponentially increases with decreasing separation between donors and acceptors. This fact usually leads to the well-known shift of the DA PL bands toward higher energy with increasing laser power because more distant pairs saturate more easily. In our case, the laser power dependence of the low-temperature PL spectrum revealed a blue shift of approximately 10 meV per decade for both B_1 and B_2 bands, clearly suggesting that these bands are related to DAP recombination. Two recombination processes were assumed to take place for B_1 and B_2 bands: (i) a deep donor to shallow acceptor transition for B_1 and (ii) a shallow donor to deep acceptor transition for the B_2 band. The DAP recombination model for these bands is presented in Figure 6.

To identify the origin of these defects, the following aspects have been considered. The obtained activation energy of E_a = 21 meV for B_1 emission indicates the presence of shallow acceptor defects. Considering that V_{Sn} represents the main native defects responsible for p-type conductivity in SnS films, we attributed this shallow acceptor to the first ionization energy of V_{Sn}, which is known to be ~20 meV.[34] For the B_2

DOI: 10.1021/acsami.9b03213
ACS Appl. Mater. Interfaces 2019, 11, 17539–17554

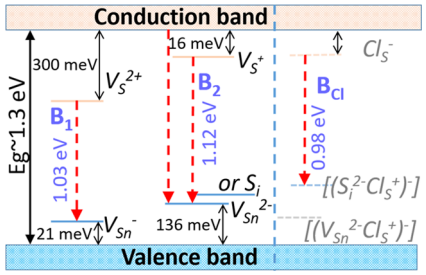

Figure 6. DAP recombination model for SnS films at 10 K vs PDT conditions.

band, we achieved E_a = 136 meV, which is compatible to the doubly ionized V_{Sn}^{2-} deep acceptor in SnS films. According to Vidal et al.,[53] the first ionization transition of the tin vacancy from V_{Sn}^{0} to V_{Sn}^{-} and the second transition from V_{Sn}^{-} to V_{Sn}^{2-} have low formation energies. The second ionization step of V_{Sn} was estimated to be ~0.2 eV from the dark conductivity studies.[10,34] Although this defect configuration has a high probability, involving only V_{Sn}^{2-} as a deep acceptor implies the pinning of the Fermi level closer to the middle of the band gap (the B_2/B_1 ratio increases with annealing temperature (Figure 7b)), meaning a decrease in the carrier concentration. In our

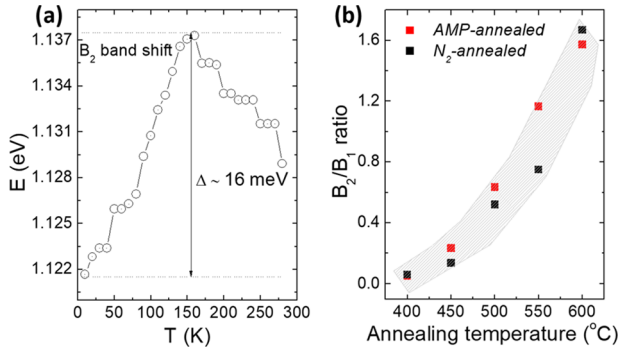

Figure 7. (a) Shift of the B_2 PL band peak position with increasing measurement temperature. (b) B_2/B_1 ratio at T = 10 K after the AMP-annealing and N_2-annealing steps at 400−600 °C for 30 min.

case, the hole density increased at elevated annealing temperatures, indicating a high concentration of $[V_{Sn}]$. Considering the high partial pressure of sulfur (due to the high solubility of sulfur in SnS) at these temperatures, the presence of the sulfur interstitial defect, S_i, is highly likely. It is assumed that S_i also acts as an acceptor since the sulfur atom in the SnS lattice has a much higher probability of accepting electrons from the valence band than of donating electrons to the conduction band. Thus, both S_i and V_{Sn}^{2-} deep acceptor defects could be involved in the B_2 emission band. It is clear that involving both V_{Sn} and S_i acceptor defects implies the existence of sulfur-rich conditions in SnS, but the hole concentration in the films is mainly determined by the overall concentration of ionized tin vacancies at the temperatures under investigation.

To identify the origin of the shallow donor level involved in B_2 emission, we analyzed the shift of this band as a function of the measurement temperature. Figure 7a shows that the B_2 band is shifted toward higher energies as the measurement temperature is increased. This is a typical situation for DAPs at relatively low temperatures. When the donor level is first occupied and as the temperature is increased, recombination occurs between the conduction band and the deep acceptor (Figure 6). The overall shift of B_2 approximates the activation energy of the donor level (~16 meV), i.e., a shallow donor (Figure 7a). Considering the high concentration of holes at elevated temperatures generated by the high concentration of $[V_{Sn}]$ in SnS films, we assume that this shallow donor is due to the singly ionized sulfur vacancies, V_S^{+}. This concept is consistent with the trend in the electrical properties. The higher the annealing temperature, the higher the sulfur partial pressure above the SnS films, the smaller the concentration of $[V_S]$, and the greater the hole density in the layers. Thus far, we have proven the nature of the donor level for the B_2 emission band.

To estimate the depth of the deep donor involved in the B_1 emission band, eq 17 was used

$$E_{B_1} = E_g - (E_D + E_A) + \frac{e^2}{\varepsilon \cdot r} \quad (17)$$

where E_{B_1} is the energy of the B_1 emission, E_g is the band gap, E_D and E_A are the depths of the donor and acceptor states, respectively, and the last term is the Coulomb term. E_D was estimated to be ~300 meV. This deep donor could be assigned to doubly ionized sulfur vacancies (V_S^{2+}), which lie close to the valence band maximum at ~0.25 eV and, therefore, do not compensate for the hole concentration generated by V_{Sn}.[53] The concentration of $[V_S^{2+}]$ is dependent on the S pressure so that if the SnS films are pushed to a high S-rich state (as is the case for high annealing temperatures), the formation energy of V_S^{2+} becomes larger, and its equilibrium concentration is reduced.[53]

We next investigated the changes in the PL spectra of SnS films induced by the $SnCl_2$-annealing step (Figure 5c). As shown previously, higher temperatures of recrystallization (450−500 °C) resulted in the formation of dense, continuous, and pore-free SnS thin films with a random orientation (SEM, XRD). The same layers exhibited improved p-type conductivity and hole mobility, suitable for application in solar cells. Considering these approaches, we chose only the $SnCl_2$-treated films at 500 °C for further PL analysis. The PL spectrum of the recrystallized SnS films exhibited a broader emission at a slightly lower energy (0.98 eV) compared to the previous annealing conditions, suggesting the incorporation of different defects. Due to the lower PL intensity, it was difficult to determine the temperature dependence for this emission band and the activation energy. Considering the incorporation of chlorine in the SnS films, the 0.98 PL emission band is most likely related to the donor−acceptor recombination between the Cl_S^{+} donor and the V_{Sn}^{2-} or S_i deep acceptors (Figures 6 and 5, B_{Cl} band). Different chlorine complex defects, such as the $[(S_i^{2-}Cl_S^{+})^{-}]$ deep acceptor complex, could also be involved in this emission band. As shown in the Electrical Properties section, a neutral defect $[(V_{Sn}^{2-}2Cl_S^{+})^{\times}]$ can be formed at high concentrations of dopant, and as a result of its dissociation (eq 14), the created shallow acceptor defect $[(V_{Sn}^{2-}Cl_S^{+})^{-}]$ compensates for the Cl_S^{+} shallow donor. These complex defects are usually formed in chlorine-doped CdS and CdTe films.[55,66,67] For the latter compounds, the Cl atom is thought to substitute for a Te or S atom and act as a shallow donor related to the formation of Cl_{Te}^{+} and Cl_S^{+} with an energy level of E_c = 10−20 meV.[55,66,67] The Cl solubility at substitutional Te/S sites at 500 °C is ~10^{17} cm^{-3}.[68] With Cd vacancies, Cl forms defects, shallow acceptors or so-called A centers $[(V_{Cd}^{-}Cl_{Te}^{+})^{-}]$ or $[(V_{Cd}^{-}Cl_S^{+})^{-}]$ at E_V = 0.12 eV, and

DOI: 10.1021/acsami.9b03213
ACS Appl. Mater. Interfaces 2019, 11, 17539−17554

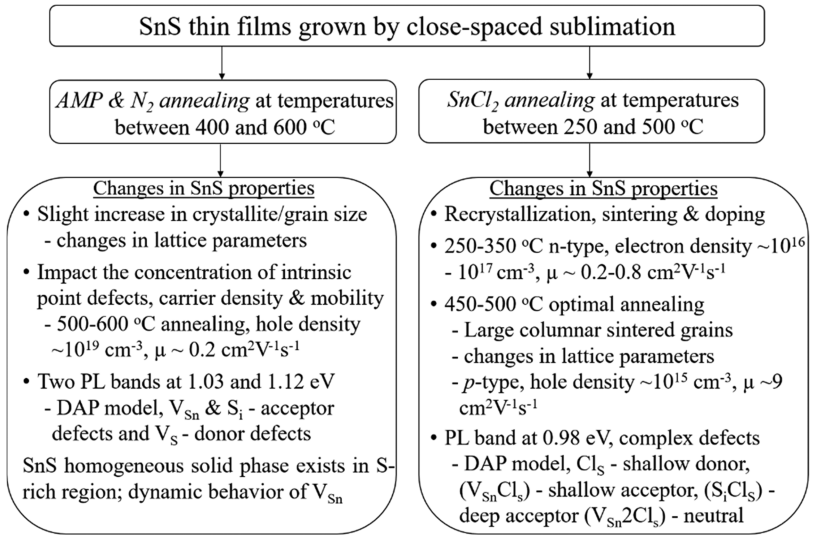

Figure 8. Summary of the impact of various PDT processes on the properties of SnS thin films.

neutral complexes $[(V_{Cd}^{2-}2Cl_{Te}^{+})^{\times}]$, $[(V_{Sn}^{2-}2Cl_{S}^{+})^{\times}]$.[55,67,69] In CdTe, Cd vacancies are deep acceptors at E_V = 0.47 eV.[67,69]

Our results seem to support these well-established processes. Thus, the hole concentration in $SnCl_2$-treated films decreases, indicating the compensation effect of the Cl_S^+ donor defect. As shown, the rate of chlorine doping is determined by the equilibrium between the liquid and solid $SnCl_2$−SnS phases at the processing temperature. At the same time, high chloride annealing temperatures of 450−500 °C promoted the removal of excess Cl from the SnS lattice, hence contributing to the stabilization of the $[(V_{Sn}^{2-}Cl_S^{+})^{-}]$ shallow acceptor defect, which was assumed to be the main defect responsible for p-type conductivity in chlorine-doped films. The changes in the lattice parameter (Table 1) indicate processes taking place inside the lattice of $SnCl_2$-treated SnS films. Thus far, the changes in the electrical and structural properties correlate well with the defect features in the photoluminescence spectra. Further PL investigations of the $SnCl_2$-annealed SnS films are necessary to prove the origin of chlorine complex defects and their impact on the electrical properties of the layers. A summary of the SnS thin-film properties influenced by various PDT processes is presented in Figure 8.

Dependence of the Solar Cell Efficiency on PDT Processes. To investigate the influence of the PDT processing conditions on the device performance, a series of 100 solar cells with a superstrate configuration of glass/FTO/CdS/SnS/Au (where FTO is fluorine-doped tin oxide) were fabricated. Figure 9a shows the cross-sectional SEM image of the stack and a representative photograph. Figure 10 shows the changes in the PV device parameters before and after the AMP-annealing and N_2-annealing steps from 400 to 600 °C. For both annealing conditions, 10 cells were used for each processing temperature and the average values of PV parameters are presented (Figure 10). The representative current density−voltage (J−V) characteristics, measured under AM 1.5 conditions, are shown in Figure 11.

The untreated solar cells exhibited a conversion efficiency (η) of ∼1% with the open-circuit voltage (V_{OC}), short-circuit current density (J_{SC}), and fill factor (FF) of 200 mV, 11.5 mA/cm^2, and 42%, respectively. Both annealing conditions at 400−450 °C promoted improvements in solar cell output characteristics, leading to V_{OC}, J_{SC}, FF, and η values of 250 mV, 14 mA/cm^2, 48%, and 1.7%, respectively. However, a further increase in the annealing temperature (≥500 °C) produced a drastic decrease in all PV parameters of the cells.

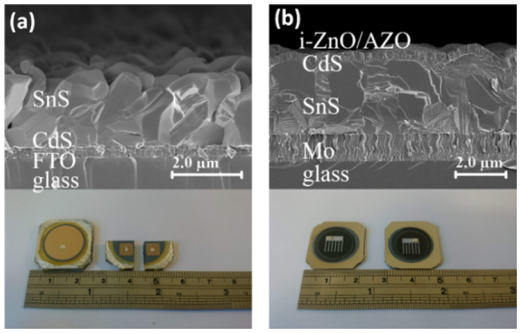

Figure 9. Cross-sectional SEM images and photographs of the (a) superstrate configuration of glass/FTO/CdS/SnS and (b) substrate configuration of glass/Mo/SnS/CdS/i-ZnO/AZO heterostructures with $SnCl_2$-annealed SnS films at 500 °C.

When explaining the impact of both annealing conditions on the device performance, the changes in the structural defects and optoelectronic properties of SnS films induced by these treatments should be considered. Although the grain size and GBs have a major impact on the device efficiency, we did not observe any evident changes in the morphology of the layers after the AMP-annealing and N_2-annealing steps at 400−600 °C. Both annealing procedures affect the concentration of intrinsic point defects and the hole density in SnS films. As shown by the variations in the PV device parameters, J_{SC} and V_{OC} are strongly influenced by the carrier collection length, the width of the space charge region (SCR), and the diffusion length. The width of the SCR in a p−n heterojunction depends on many factors, but among these parameters, the carrier concentration is crucial in both n-type and p-type components. Generally, the SCR is virtually located in the semiconductor, which has a low carrier density, usually in the p-type absorber. For example, in CdTe and CIGS TFSC, where the p−n junction is basically formed between the n-type transparent conducting oxide (TCO)/CdS window and the p-type absorber, the SCR extends mainly in the absorber material with a higher resistivity and a lower carrier density (low doping

DOI: 10.1021/acsami.9b03213
ACS Appl. Mater. Interfaces 2019, 11, 17539−17554

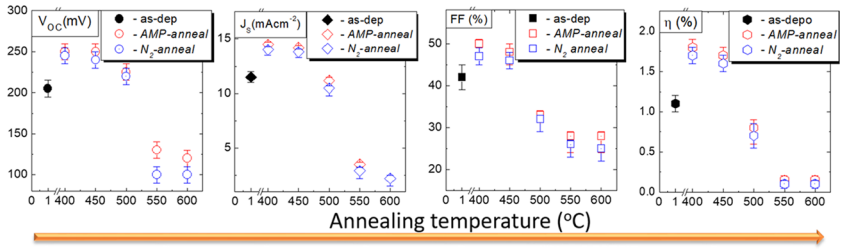

Figure 10. PV parameters of the superstrate configuration of glass/FTO/CdS/SnS/Au solar cells before and after AMP-annealing and N_2-annealing at temperatures between 400 and 600 °C for 30 min. For both annealing conditions, 10 cells were used for each processing temperature and the average values of PV parameters are presented.

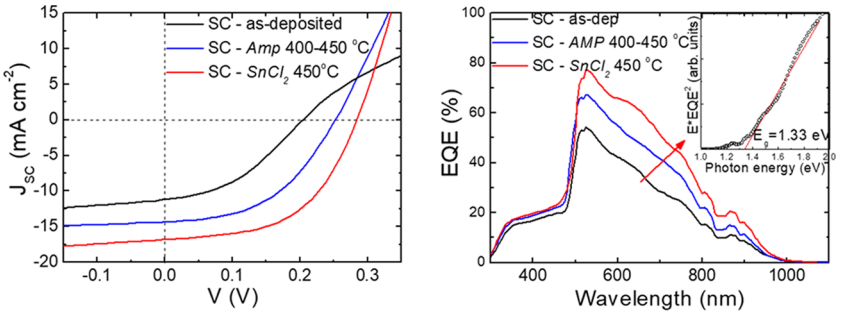

Figure 11. *J*–*V* characteristics and EQE spectra of three solar cells (SCs): superstrate configuration of glass/FTO/CdS/SnS/Au SC with as-deposited (black curve) and AMP/N_2-annealed SnS films for 30 min (blue curve); substrate configuration of glass/Mo/SnS/CdS/i-ZnO/AZO/Ni/Al SC with $SnCl_2$-annealed SnS films at 450 °C for 30 min (red curve). The inset shows the modified EQE plot, giving a band gap estimation of 1.33 eV of SnS at RT.

level, 10^{14}–10^{16} cm^{-3}) than those of the n-type partner (10^{18}–10^{20} cm^{-3}).[70] The ideal electron density for the n-type layer is 1–2 orders of magnitude above the hole concentration in the absorber material, assuming the existence of an ideal 0.2–0.4 eV conduction band spike offset between the p-type and n-type layers.[71] This configuration also provides a major advantage since the absorption starts in the SCR, which is the main region where the photogenerated electron–hole pairs are effectively separated, giving rise to the short-circuit current and voltage.

In our case, the electron density in the CSS CdS layer is much lower (10^{12}–10^{13} cm^{-3}) than that of the SnS absorber (~10^{17} cm^{-3}) so that the SCR is very narrow and most likely extends into the window layer at the CdS/SnS interface, leading to ineffective charge separation, high recombination rates, and poor performance for the untreated solar cells. Annealing at 400–450 °C seems to promote conditions for better lattice matching at the CdS–SnS interface, hence improving the quality of the electrical p–n junction. A balanced carrier concentration and the increased mobility improve the cell efficiency. The improved mobility likely reduces the carrier recombination. The above conclusions are supported by the changes in the external quantum efficiency (EQE) spectra of the SnS/CdS solar cells (Figure 11b). Thus, the untreated solar cell showed a decreased EQE response in the long-wavelength (600–800 nm) regions due to the short carrier diffusion length and/or the narrow SCR. The EQE response showed evidence for improved carrier collection after the AMP-annealing and N_2-annealing steps at 400–450 °C (Figure 11b).

The hole concentration increased in the SnS films (~10^{19} cm^{-3}) as the temperature of AMP-annealing and N_2-annealing increased (Figure 3a). This increase would have the effect of shrinking the width of the SCR, thereby decreasing the carrier collection length and decreasing the device output (Figure 10).

Following our ambitious goal to prove the applicability of $SnCl_2$ PDT in SnS solar cells, we next investigated the impact of this processing step on the device performance. In the first stage of the experiment, we encountered some difficulties. We observed the disappearance of the CdS buffer layer after the $SnCl_2$-annealing step at 450–500 °C for 30 min. This effect was present even at low annealing temperatures of 250–300 °C. In addition, we observed side effects from annealing, such as the precipitation of yellow-brown CdS–$SnCl_2$ in the cold regions of the ampules. In the case with only SnS single layers, white $SnCl_2$ residuals in the cold part of the ampule were detected in the same treatment step. Following the experimental evidence of CdS precipitation, we analyzed the possible thermodynamic reaction in the $SnCl_2$–CdS–SnS system (eq 18)

$$SnCl_{2(l)} + CdS_{(s)} \rightarrow CdCl_{2(s)} + SnS_{(s)},\ \Delta G(250\ °C) = -2.7\ \text{kcal/mol} \quad (18)$$

According to the thermodynamically favored eq 18, the equilibrium is shifted toward the formation of solid $CdCl_2$ and SnS species over the entire temperature interval (250–500 °C). The Gibbs free energy (ΔG) is negative, and even with an increasing annealing temperature, ΔG tends to be positive (Table S1 in the Supporting Information); at 500 °C, $\Delta G < 1$, indicating the predominant formation of $CdCl_2$ and SnS. This finding is also supported by the equilibrium constant, showing that the molar concentration of the reaction products is higher than that of the reactants over the entire temperature interval (Table S1 in the Supporting Information). The melting point of $CdCl_2$ is ~567 °C, while the eutectic temperature of CdS–$CdCl_2$ is ca. 515–520 °C.[72] The melting point of $SnCl_2$,

DOI: 10.1021/acsami.9b03213
ACS Appl. Mater. Interfaces 2019, 11, 17539–17554

$SnCl_2$–SnS,[46] and eutectic $CdCl_2$–$SnCl_2$[73] is lower than 247 °C. Both $SnCl_2$ and $CdCl_2$ have high partial vapor pressures in the temperature range of 250–500 °C,[48,74] where the intensive recrystallization and sintering of SnS and CdS occur. These facts indicate the high solubility of CdS in the $SnCl_2$–$CdCl_2$–SnS melted flux and thereby its excessive consumption during the chloride treatment step. These results indicate that the $SnCl_2$ treatment is not applicable for the superstrate configuration of SnS/CdS/TCO. However, this approach would be appropriate for solar cells in a substrate configuration.

For a proof-of-concept demonstration, a series of solar cells were fabricated with the glass/Mo/SnS/CdS/i-ZnO/Al:ZnO/Ni/Al substrate configuration (see Experimental Section). From various annealing temperatures used for the $SnCl_2$-annealing step, only SnS films treated at 450–500 °C for 30 min were used in substrate configuration solar cells because at these temperatures, SnS films with more suitable properties for solar cell application could be obtained. Figure 11 shows the J–V curve for a glass/Mo/SnS/CdS/i-ZnO/Al:ZnO/Ni/Al solar cell with a $SnCl_2$-annealed SnS film at 450 °C. It is evident that the treatment produced significant improvements in the device performance. It should be noted that the untreated substrate configuration cells exhibited a conversion efficiency between 1 and 1.1%, comparable to the untreated superstrate device performance (as deposited solar cell in Figure 11). The cross-sectional SEM image and plan view of the substrate configuration stack are shown in Figure 9b. The contributions of large, columnar, and sintered SnS grains with enhanced mobility and a balanced carrier concentration improved the V_{OC}, J_{SC}, FF, and conversion efficiency up to 290 mV, 17.2 mA/cm^2, 56%, and 2.8%, respectively. For the same device, the EQE measurements clearly indicate improvements over almost the entire spectrum, implying better collection efficiency (Figure 11). The enhancements in V_{OC} and FF are clearly determined by the decrease in the density of GBs and pinholes, leading to decreased recombination rates in the SCR. These results, together with the enhanced carrier mobility and balanced carrier concentration, lead to improvements in the carrier collection, thereby improving the J_{SC} and conversion efficiency. Following the achieved 2.8% efficiency of the solar cells with a substrate configuration of glass/Mo/SnS/CdS/i-ZnO/Al:ZnO/Ni/Al, substantial room remains for device improvement. This improvement may involve the optimization of the $SnCl_2$-annealing step in the temperature range of 450–500 °C by controlling the duration of annealing and the concentration of chloride flux. The chloride processing step could be performed in one, two, or even more subsequent steps to obtain SnS films with large columnar and sintered grains. The chlorine concentration in the films could be controlled by subsequent AMP-annealing or N_2-anneling steps in the process tube under a narrow temperature gradient. The high partial vapor pressure of $SnCl_2$ allows an efficient accumulation of chloride excess from the SnS lattice. The ideal case for chloride-treated SnS films would be to obtain large columnar sintered grains with a concentration of Cl dopant in the range of 10^{16}–(5×10^{16}) cm^{-3}, which is assumed to be the optimal concentration to provide a hole density within the same range. This is a well-established technology for CdTe, where chloride is an active agent for recrystallization and sintering acts as a dopant to promote p-type conductivity in CdTe. As shown above, during doping, chlorine associates with Cd vacancies, forming shallow acceptor centers $[(V_{Cd}^{-2}Cl_{Te}^{+})^{-}]$ at E_V = 0.12 eV,[67,69] thereby improving the hole density in CdTe. This process has a great advantage since the formation of such a complex annihilates the contribution of Cd vacancy deep acceptors at E_V = 0.47 eV.[67,69] The presence of deep acceptor states in CdTe, CIGS, SnS, and other p-type absorbers is known to be detrimental for efficient solar cells. Thus far, the optimized chlorine doping in CdTe has enabled an efficiency as high as 15%.[75] In SnS, we expect to observe a similar effect in which chlorine doping generates an associated $[(V_{Sn}^{-2}Cl_S^{+})^{-}]$ shallow acceptor complex, removing the contributions of $[V_{Sn}^{2-}]$ deep acceptors, improving the hole carrier density and mobility in SnS films and enhancing the device performance. The optimization of the buffer layer is also a promising and active area of research. Thus, in addition to adopting conventional strategies such as H_2S treatment and optimizing interface band alignment with more suitable n-type buffer layers, a chloride treatment could be a formidable approach for making further progress in the efficiency of SnS TFSCs.

CONCLUSIONS

A systematic study of changes in the properties of CSS SnS thin films and SnS/CdS solar cells induced by PDT processes, including the AMP-annealing, N_2-annealing, and $SnCl_2$-annealing steps, was carried out to understand the physicochemical mechanisms of the processes and to optimize the device efficiency.

The AMP-annealing and N_2-annealing conditions at temperatures between 400 and 600 °C did not affect the grain size or GB density of the SnS layers but significantly impacted the concentration of intrinsic point defects, hole carrier density, and mobility in the films. No secondary phases were detected by XRD and Raman analyses for both the as-deposited SnS films and after any of the PDT processes. Annealing at 400 and 450 °C enhanced the hole mobility in SnS films, promoted conditions for better lattice matching at the CdS–SnS interface, improved the quality of the electrical p–n junction, and hence, enhanced the solar cell efficiency. High annealing temperatures (500–600 °C) promoted rearrangement of the SnS lattice, strongly enhanced the hole concentration to the level of 10^{19} cm^{-3}, and decreased the carrier mobility, which had a detrimental impact on the solar cell performance. For the same interval of annealing temperatures, the PL spectra showed two distinct emission bands, B_1 and B_2. The experimental results for these PL bands could be consistently explained by the DAP model, which involved V_{Sn} acceptor defects and V_S donor defects. Changes in the properties of SnS films induced by AMP-annealing and N_2-annealing processes were explained based on the claim that the SnS homogeneous solid phase exists only in the sulfur-rich region and by the dynamic behavior of tin vacancies prevailing under sulfur-rich conditions.

The $SnCl_2$-annealing step at temperatures between 250 and 500 °C promoted grain growth and sintering, especially at 450 and 500 °C. The changes in the lattice parameter accompanied by displacement of the main (111) XRD peak indicated the incorporation of chlorine and the formation of tin vacancies inside the lattice of $SnCl_2$-treated SnS films. The recrystallized films at 250 and 300 °C exhibited n-type conductivity and low Hall mobility. The p-type conductivity was restored, and the Hall mobility improved as the $SnCl_2$ annealing temperature was increased from 350 to 500 °C. The broader PL emission at a slightly lower energy (0.98 eV) compared to the previous

DOI: 10.1021/acsami.9b03213
ACS Appl. Mater. Interfaces 2019, 11, 17539–17554

annealing conditions suggested the incorporation of chlorine defects.

Based on these systematic results, it is claimed that the $SnCl_2$ treatment process induced the formation of a liquid flux and mass transport through the melted phase, promoting grain growth by recrystallization and sintering. The grain growth was accomplished by incorporating flux components (doping) into the growing SnS lattice under saturation concentrations according to the distribution coefficient between the liquid and solid phases at the processing temperature. For the first time, a comprehensive understanding of the evolution of the structural, electrical, and optical properties of SnS as a result of the SnS−$SnCl_2$ treatment process was obtained. We experimentally demonstrated that SnS/CdS solar cells with an efficiency of ∼2.8% can be achieved by recrystallization of SnS films in the presence of a $SnCl_2$ melted flux. Following these achievements, additional systematic work is required to further improve the efficiency of this novel device.

■ ASSOCIATED CONTENT

Supporting Information

The Supporting Information is available free of charge on the ACS Publications website at DOI: 10.1021/acsami.9b03213.

Close-spaced sublimation system for thin-film deposition; substrate cleaning procedure; standardization of SnS source material; SEM images of N_2 and AMP-annealed SnS films; morphology analysis of $SnCl_2$-annealed CSS SnS thin films; high-resolution XRD data of the (111) peak for N_2 and AMP-annealed films; Raman spectra of SnS films depending on PDT processes; and thermodynamic aspects in the $SnCl_2$−CdS−SnS system (PDF)

■ AUTHOR INFORMATION

Corresponding Author

*E-mail: nicolae.spalatu@taltech.ee.

ORCID

Nicolae Spalatu: 0000-0003-0234-2170

Olga Volobujeva: 0000-0002-3844-2555

Notes

The authors declare no competing financial interest.

■ ACKNOWLEDGMENTS

The study was financially supported by the Estonian Ministry of Education and Research IUT19-4, IUT19-28 and by the European Regional Development Fund project: TK141 Centre of Excellence "Advanced materials and high-technology devices for sustainable energetics, sensorics and nanoelectronics" (1.01.2015−1.03.2023).

■ REFERENCES

(1) Murugadoss, V.; Wang, N.; Tadakamalla, S.; Wang, B.; Guo, Z.; Angaiah, S. In Situ Grown Cobalt Selenide/Graphene Nanocomposite Counter Electrodes for Enhanced Dye-Sensitized Solar Cell Performance. *J. Mater. Chem. A* **2017**, *5*, 14583−14594.

(2) Singh, N.; Murugadoss, V.; Nemala, S.; Mallick, S.; Angaiah, S. $Cu_2ZnSnSe_4$ QDs Sensitized Electrospun Porous TiO_2 Nanofibers as Photoanode for High Performance QDSC. *Sol. Energy* **2018**, *171*, 571−579.

(3) Yang, L.; Wang, X.; Mai, X.; Wang, T.; Wang, C.; Li, X.; Murugadoss, V.; Shao, Q.; Angaiah, S.; Guo, Z. Constructing Efficient Mixed-Ion Perovskite Solar Cells Based on TiO_2 Nanorod Array. *J. Colloid Interface Sci.* **2019**, *534*, 459−468.

(4) Poortmans, J.; Arkhipov, V. *Thin Film Solar Cells Fabrication, Characterization and Applications*; John Wiley & Sons, Ltd.: Belgium, 2008.

(5) Solar Frontier Press Release Solar Frontier Achieves World Record Thin-Film Solar Cell Efficiency of 22.9% (accessed May, 2018). http://www.solar-frontier.com/eng/news/2017/1220_press.html.

(6) Green, M. A.; Hishikawa, Y.; Warta, W.; Dunlop, E. D.; Levi, D. H.; Hohl-Ebinger, J.; Ho-Baillie, A. W. H. Solar Cell Efficiency Tables (Version 50). *Prog. Photovoltaics* **2017**, *25*, 668−676.

(7) Wang, W.; Winkler, M. T.; Gunawan, O.; Gokmen, T.; Todorov, T. K.; Zhu, Y.; Mitzi, D. B. Device Characteristics of CZTSSe Thin-Film Solar Cells with 12.6% Efficiency. *Adv. Energy Mater.* **2014**, *4*, No. 1301465.

(8) Redinger, A.; Berg, D. M.; Dale, P. J.; Siebentritt, S. The Consequences of Kesterite Equilibria for Efficient Solar Cells. *J. Am. Chem. Soc.* **2011**, *133*, 3320−3323.

(9) Reddy, K. T. R.; Reddy, N. K.; Miles, R. W. Photovoltaic Properties of SnS Based Solar Cells. *Sol. Energy Mater. Sol. Cells* **2006**, *90*, 3041−3046.

(10) Noguchi, H.; Setiyadi, A.; Tanamura, H.; Nagatomo, T.; Omoto, O. Characterization of Vacuum-Evaporated Tin Sulfide Film for Solar Cell Materials. *Sol. Energy Mater. Sol. Cells* **1994**, *35*, 325−331.

(11) Shockley, W.; Queisser, H. J. Detailed Balance Limit of Efficiency of p-n Junction Solar Cells. *J. Appl. Phys.* **1961**, *32*, 510−519.

(12) Sinsermsuksakul, P.; Sun, L.; Lee, S. W.; Park, H. H.; Kim, S. B.; Yang, C.; Gordon, R. G. Overcoming Efficiency Limitations of SnS-Based Solar Cells. *Adv. Energy Mater.* **2014**, *4*, No. 1400496.

(13) Reddy, N.; Reddy, K. T. R. In *Tin Sulphide Films for Solar Cell Application*, Conference Record of the 26th IEEE Photovoltaic Specialists Conference, Anaheim, CA, Sept 29−Oct 3, 1997; IEEE: Piscataway, NJ, 1997.

(14) Schneikart, A.; Schimper, H. J.; Klein, A.; Jaegermann, W. Efficiency Limitations of Thermally Evaporated Thin-Film SnS Solar Cells. *J. Phys. D: Appl. Phys.* **2013**, *46*, No. 305109.

(15) Di Mare, S.; Menossi, D.; Salavei, A.; Artegiani, E.; Piccinelli, F.; Kumar, A.; Mariotto, G.; Romeo, A. SnS Thin Film Solar Cells: Perspectives and Limitations. *Coatings* **2017**, *7*, No. 34.

(16) Sinsermsuksakul, P.; Hartman, K.; Kim, S. B.; Heo, J.; Sun, L.; Park, H. H.; Chakraborty, R.; Buonassisi, T.; Gordon, R. G. Enhancing the Efficiency of SnS Solar Cells via Band-Offset Engineering with a Zinc Oxysulfide Buffer Layer. *Appl. Phys. Lett.* **2013**, *102*, No. 053901.

(17) Kawano, Y.; Chantana, J.; Minemoto, T. Impact of Growth Temperature on the Properties of SnS Film Prepared by Thermal Evaporation and its Photovoltaic Performance. *Curr. Appl. Phys.* **2015**, *15*, 897−901.

(18) Ikuno, T.; Suzuki, R.; Kitazumi, K.; Takahashi, N.; Kato, N.; Higuchi, K. SnS Thin Film Solar Cells With $Zn_{1-x}Mg_xO$ Buffer Layers. *Appl. Phys. Lett.* **2013**, *102*, No. 193901.

(19) Yago, A.; Sasagawa, S.; Akaki, Y.; Nakamura, S.; Oomae, H.; Katagiri, H.; Araki, H. Comparison of Buffer Layers on SnS Thin-Film Solar Cells Prepared by Co-Evaporation. *Phys. Status Solidi C* **2017**, *14*, No. 1600194.

(20) Lim, D.; Heo, J. Facile Strategy for the Formation of Tin Monosulfide Thin Films by Rapid Thermal Annealing. *Mater. Lett.* **2017**, *205*, 102−105.

(21) Steinmann, V.; Brandt, R. E.; Buonassisi, T. Controlled Growth of Non-Cubic, Anisotropic Solar Cell Materials, such as Antimony Selenide, is Bringing New Opportunities for Efficient Thin-Film Photovoltaics. *Nat. Photonics* **2015**, *9*, 355−357.

(22) Steinmann, V.; Chakraborty, R.; Rekemeyer, P. H.; Hartman, K.; Brandt, R. E.; Polizzotti, A.; Yang, C.; Moriarty, T.; Gradečak, S.; Gordon, R. G.; Buonassisi, T. A Two-Step Absorber Deposition Approach to Overcome Shunt Losses in Thin Film Solar Cells: Using

Tin Sulfide as a Proof-of-Concept Material System. *ACS Appl. Mater. Interfaces* **2016**, *8*, 22664−22670.
(23) Reddy, K. T. R.; Reddy, P. P.; Miles, R. W.; Datta, P. K. Investigations on SnS Films Deposited by Spray Pyrolysis. *Opt. Mater.* **2001**, *17*, 295−298.
(24) Jiang, T.; Ozin, G. A. New Directions in Tin Sulfide Materials Chemistry. *J. Mater. Chem.* **1998**, *8*, 1099−1108.
(25) Burton, L. A.; Walsh, A. Band Alignment in SnS Thin-Film Solar Cells: Possible Origin of the Low Conversion Efficiency. *Appl. Phys. Lett.* **2013**, *102*, No. 132111.
(26) Scragg, J. J.; Wätjen, J. T.; Edoff, M.; Ericson, T.; Kubart, T.; Platzer-Björkman, C. A Detrimental Reaction at the Molybdenum Back Contact in $Cu_2ZnSn(S,Se)_4$ Thin-Film Solar Cells. *J. Am. Chem. Soc.* **2012**, *134*, 19330−19333.
(27) Iguchi, Y.; Sugiyama, T.; Inoue, K.; Yanagi, H. Segregation of Chlorine in n-Type Tin Monosulfide Ceramics: Actual Chlorine Concentration for Carrier-Type Conversion. *Appl. Phys. Lett.* **2018**, *112*, No. 202102.
(28) Lin, S.; Li, X.; Pan, H.; Chen, H.; Li, X.; Li, Y.; Zhou, J. Numerical Analysis of SnS Homojunction Solar Cell. *Superlattices Microstruct.* **2016**, *91*, 375−382.
(29) Lim, D.; Suh, H.; Suryawanshi, M.; Song, G. Y.; Cho, J. Y.; Kim, J. H.; Jang, J. H.; Jeon, C. W.; Cho, A.; Ahn, S.; Heo, J. Kinetically Controlled Growth of Phase-Pure SnS Absorbers for Thin Film Solar Cells: Achieving Efficiency Near 3% with Long-Term Stability Using an SnS/CdS Heterojunction. *Adv. Energy Mater.* **2018**, *8*, No. 1702605.
(30) Rose, D.; Powell, R.; Jayamaha, U.; Maltby, M.; Giolando, D.; McMaster, A.; Kormanyos, K.; Faykosh, G.; Klopping, J.; Dorer, G. In *R&D of CdTe-Absorber Photovoltaic Cells, Modules, and Manufacturing Equipment: Plan and Progress to 100 MW/yr*, Conference Record of the 28th IEEE Photovoltaic Specialists Conference; IEEE: New York, 2000.
(31) Amarasinghe, M.; Colegrove, E.; Moseley, J.; Moutinho, H.; Albin, D.; Duenow, J.; Jensen, S.; Kephart, J.; Sampath, W.; Sivananthan, S.; Al-Jassim, M.; Metzger, W. K. Obtaining Large Columnar CdTe Grains and Long Lifetime on Nanocrystalline CdSe, MgZnO, or CdS Layers. *Adv. Energy Mater.* **2018**, *8*, No. 1702666.
(32) Ray, S. C.; Karanjai, M. K.; DasGupta, D. Structure and Photoconductive Properties of Dip-Deposited SnS and SnS_2 Thin Films and Their Conversion to Tin Dioxide by Annealing in Air. *Thin Solid Films* **1999**, *350*, 72−78.
(33) Naidu, R.; Loorits, M.; Kärber, E.; Volobujeva, O.; Raudoja, J.; Maticiuc, N.; Bereznev, S.; Mellikov, E. Impact of Vacuum and Nitrogen Annealing on HVE SnS Photoabsorber Films. *Mater. Sci. Semicond. Process.* **2017**, *71*, 252−257.
(34) Rau, H. High Temperature Equilibrium of Atomic Disorder in SnS. *J. Phys. Chem. Solids* **1966**, *27*, 761−769.
(35) Yue, G. H.; Wang, W.; Wang, L. S.; Wang, X.; Yan, P. X.; Chen, Y.; Peng, D. L. The Effect of Anneal Temperature on Physical properties of SnS films. *J. Alloys Compd.* **2009**, *474*, 445−449.
(36) Hartman, K. Annealing for Intrinsic Point-Defect Control and Enhanced Solar Cell Performance: The Case of H_2S and Tin Sulfide (SnS). Ph.D. Thesis, Massachusetts Institute of Technology: Cambridge, 2015.
(37) Paudel, N. R.; Xiao, C.; Van, Y. In *Study of Close Space Sublimation (CSS) Grown SnS Thin-Films for Solar Cell Applications*, 42nd IEEE Photovoltaic Specialists Conference, New Orleans, Louisiana, 14−19 June, 2015; IEEE: New Orleans, LA, 2015.
(38) Di Mare, S.; Salavei, A.; Menossi, D.; Piccinelli, F.; Bernardi, P.; Artegiani, E.; Kumar, A.; Mariotto, G.; Romeo, A. In *A Study of SnS Recrystallization by Post Deposition Treatment*, 2016 IEEE 43rd Photovoltaic Specialists Conference (PVSC), Portland, OR, June 5−10, 2016; IEEE, 2016.
(39) Steinmann, V.; Brandt, R. E.; Chakraborty, R.; Jaramillo, R.; Young, M.; Ofori-Okai, B. K.; Yang, C.; Polizzotti, A.; Nelson, K. A.; Gordon, R. G.; Buonassisi, T. The Impact of Sodium Contamination in Tin Sulfide Thin-Film Solar Cells. *APL Mater.* **2016**, *4*, No. 026103.
(40) Timmo, K.; Kauk-Kuusik, M.; Pilvet, M.; Mikli, V.; Kärber, E.; Raadik, T.; Leinemann, I.; Altosaar, M.; Raudoja, J. Comparative Study of SnS Recrystallization in Molten CdI_2, $SnCl_2$ and KI. *Phys. Status Solidi C* **2016**, *13*, 8−12.
(41) Yanuar, F.; Guastavino, C.; Llinares, C. E.; Djessas, K.; Masse, G. SnS Thin Films Grown by Close-Spaced Vapor Transport. *J. Mater. Sci. Lett.* **2000**, *19*, 2135−2137.
(42) Zhao, L.; Di, Y.; Yan, C.; Liu, F.; Cheng, Z.; Jiang, L.; Hao, X.; Lai, Y.; Li, J. In Situ Growth of SnS Absorbing Layer by Reactive Sputtering for Thin Film Solar Cells. *RSC Adv.* **2016**, *6*, 4108−4115.
(43) Eckertova, L. *Physics of Thin Films*, 2nd ed.; Plenum Publishing Corporation: New York, 1986.
(44) Major, J. D.; Durose, K. Early Stage Growth Mechanisms of CdTe Thin Films Deposited by Close Space Sublimation for Solar Cells. *Sol. Energy Mater. Sol. Cells* **2011**, *95*, 3165−3170.
(45) Piacente, V.; Foglia, S.; Scardala, P. Sublimation Study of the Tin Sulphides SnS_2, Sn_2S_3 and SnS. *J. Alloys Compd.* **1991**, *177*, 17−30.
(46) Blachnik, R.; Kasper, F. W. Tin(II)Halide−Tin(II)-Chalcogenide Systems. *Z. Naturforsch. B* **1974**, *29*, 159−162.
(47) Spalatu, N.; Krunks, M.; Hiie, J. Structural and Optoelectronic Properties of $CdCl_2$ Activated CdTe Thin Films Modified by Multiple Thermal Annealing. *Thin Solid Films* **2017**, *633*, 106−111.
(48) Spalatu, N. Development of CdTe Absorber Layer for Thin-Film Solar Cells. Ph.D. Thesis, Tallinn University of Technology: Tallinn, Estonia, 2017.
(49) Cordero, B.; Gómez, V.; Platero-Prats, A. E.; Revés, M.; Echeverría, J.; Cremades, E.; Barragán, F.; Alvarez, S. Covalent Radii Revisited. *Dalton Trans.* **2008**, 2832−2838.
(50) Albers, W.; Schol, K. The P-T-X Phase Diagram of the System Sn-S. *Philips Res. Rep.* **1961**, *16*, 329−342.
(51) Cardona, M. *Light Scattering in Solids*; Springer-Verlag: Berlin, 1983.
(52) Albers, W.; Haas, C.; Vink, H. J.; Wasscher, J. D. Investigations on SnS. *J. Appl. Phys.* **1961**, *32*, 2220−2225.
(53) Vidal, J.; Lany, S.; d'Avezac, M.; Zunger, A.; Zakutayev, A.; Francis, J.; Tate, J. Band-Structure, Optical Properties, and Defect Physics of the Photovoltaic Semiconductor SnS. *Appl. Phys. Lett.* **2012**, *100*, No. 032104.
(54) Gode, F.; Guneri, E.; Baglayan, O. Effect of Tri-Sodium Citrate Concentration on Structural, Optical and Electrical Properties of Chemically Deposited Tin Sulfide Films. *Appl. Surf. Sci.* **2014**, *318*, 227−233.
(55) Altosaar, M. E.; Kukk, P. L.; Hiie, J. V. Chlorine Solubility in CdS and the Structure of CdS-Cl Point Defects. *J. Inorg. Chem.* **1983**, *28*, 69−75.
(56) Marfaing, Y. Impurity Doping and Compensation Mechanisms in CdTe. *Thin Solid Films* **2001**, *387*, 123−128.
(57) Wilson, I. D.; Adlard, E. R.; Cooke, M.; Poole, C. F. *Encyclopedia of Separation Science*, 1st ed.; Academic Press: London, U.K., 2000.
(58) Terheggen, M.; Heinrich, H.; Kostorz, G.; Romeo, A.; Baetzner, D.; Tiwari, A. N.; Bosio, A.; Romeo, N. Structural and Chemical Interface Characterization of CdTe Solar Cells by Transmission Electron Microscopy. *Thin Solid Films* **2003**, *431−432*, 262−266.
(59) Durose, K.; Cousins, M. A.; Boyle, D. S.; Beier, J.; Bonnet, D. Grain Boundaries and Impurities in CdTe/CdS Solar Cells. *Thin Solid Films* **2002**, *403−404*, 396−404.
(60) Harvey, S. P.; Teeter, G.; Moutinho, H.; Al-Jassim, M. M. Direct Evidence of Enhanced Chlorine Segregation at Grain Boundaries in Polycrystalline CdTe Thin Films via Three-Dimensional TOF-SIMS Imaging. *Prog. Photovoltaics* **2015**, *23*, 838−846.
(61) Iguchi, Y.; Inoue, K.; Sugiyama, T.; Yanagi, H. Single-Crystal Growth of Cl-Doped n-Type SnS Using $SnCl_2$ Self-Flux. *Inorg. Chem.* **2018**, *57*, 6769−6772.
(62) Sajeesh, T. H.; Poornima, N.; Kartha, C. S.; Vijayakumar, K. P. Unveiling the Defect Levels in SnS Thin Films for Photovoltaic

DOI: 10.1021/acsami.9b03213
ACS Appl. Mater. Interfaces 2019, 11, 17539−17554

Applications Using Photoluminescence Technique. *Phys. Status Solidi A* **2010**, *207*, 1934−1939.
(63) Warrier, A. R.; Gandhimathi, R. Surface Plasmon Resonance Induced Enhancement of Photoluminescence and Raman Line Intensity in SnS Quantum Dot-Sn Nanoparticle Hybrid Structure. *Methods Appl. Fluoresc.* **2018**, *6*, No. 035009.
(64) Manukumar, K. N.; Nagaraju, G.; Kishore, B.; Madhu, C.; Munichandraiah, N. Ionic Liquid-Assisted Hydrothermal Synthesis of SnS Nanoparticles: Electrode Materials for Lithium Batteries, Photoluminescence and Photocatalytic Activities. *J. Energy Chem.* **2018**, *27*, 806−812.
(65) Krustok, J.; Collan, H.; Hjelt, K. Does the Low-Temperature Arrhenius Plot of the Photoluminescence Intensity in CdTe Point Towards an Erroneous Activation Energy. *J. Appl. Phys.* **1997**, *81*, 1442−1445.
(66) Desnica, U. V. Doping Limits in II-VI Compounds-Challenges, Problems and Solutions. *Prog. Cryst. Growth Charact. Mater.* **1998**, *36*, 291−357.
(67) Castaldini, A.; Cavallini, A.; Fraboni, B.; Fernandez, P.; Piqueras, J. Deep Energy Levels in CdTe and CdZnTe. *J. Appl. Phys.* **1998**, *83*, 2121−2126.
(68) Shaw, D.; Watson, E. The Diffusion of Chlorine in CdTe. *J. Phys. C: Solid State Phys.* **1984**, *17*, 4945−4950.
(69) Valdna, V. P-Type Doping of CdTe. *Solid State Phenom.* **1999**, *67*−*68*, 309−314.
(70) Reinders, A.; Verlinden, P.; Sark, W. V.; Freundlich, A. *Photovoltaic Solar Energy from Fundamentals to Applications*; John Wiley & Sons, Ltd.: U.K., 2017.
(71) Niemegeers, A.; Burgelman, M.; De Vos, A. On the CdS/$CuInSe_2$ Conduction Band Discontinuity. *Appl. Phys. Lett.* **1995**, *67*, 843−845.
(72) Tomashyk, V. *Quaternary Alloys Based on II*−*VI Semiconductors*; CRS Press, Taylor & Francis Group: LLC, New York, 2014.
(73) Herrmann, G. Über die Verbindungsfähigkeit der Chloride von Cu, Pb, Fe, Zn, Sn und Bi und über die Verbindungsfähigkeit der Chloride, Bromide und Jodide von Cu und Cd und die Lichtempfindlichkeit ihrer Mischkristalle. *Z. Anorg. Chem.* **1911**, *71*, 257−302.
(74) Lide, D. R. *Handbook of Chemistry and Physics*; CRC Press: New York, 1998.
(75) Basol, B. M.; McCandless, B. Brief Review of Cadmium Telluride-Based Photovoltaic Technologies. *J. Photonics Energy* **2014**, *4*, No. 040996.

DOI: 10.1021/acsami.9b03213
ACS Appl. Mater. Interfaces 2019, 11, 17539−17554